Multiscale Modeling of Methane Catalytic Partial Oxidation: From the Mesopore to the Full-Scale Reactor Operation

Jorge E. P. Navalho, José M. C. Pereira, and José C. F. Pereira
LAETA, IDMEC, Instituto Superior Técnico, Universidade de Lisboa,
Av. Rovisco Pais 1, 1049-001 Lisbon, Portugal

DOI 10.1002/aic.15945
Published online September 21, 2017 in Wiley Online Library (wileyonlinelibrary.com)

A multiscale methodology combining three different reactor length-scales is presented to investigate the role of the catalyst internal pore structure and metal loading and dispersion on the catalyst layer and full-scale reactor performances. At the catalyst level, the methodology involves pore-scale simulations in the three-dimensional mesopore and macropore space. The information gathered at the catalyst level is delivered to the full-scale reactor model. The methodology is applied to a honeycomb reactor performing methane partial oxidation considering reaction kinetics described through a detailed multistep reaction mechanism. Realistic mesopore and macropore structures were reconstructed and combined to form specific bidisperse porous washcoat layers. The study shows that species effective diffusivities vary significantly but not in the same proportion for different structures. For structures featuring poor transport characteristics, the integral methane conversion and hydrogen selectivity are strongly affected while the reactor temperatures increase substantially. © 2017 American Institute of Chemical Engineers *AIChE J*, 64: 578–594, 2018
Keywords: multiscale modeling, porous catalysts, effective diffusion coefficients, diffusion and reaction, catalytic partial oxidation

Introduction

Catalytic partial oxidation (CPOx) of methane has been recognized as a competitive reaction route for synthesis gas (mixture composed by H_2 and CO) production. Synthesis gas generated from methane CPOx can be used as feedstock for liquid fuel (Fischer-Tropsch), methanol and ammonia syntheses,[1,2] as well as for (CO–tolerant) fuel cells (SOFC).[3,4] High purity H_2 production can also be obtained by forwarding the synthesis gas stream to downstream upgrading and purification stages.[2,4] Partial oxidation of methane can be carried out in small, compact, and simple (structured or unstructured) reactors, with high throughputs and low thermal inertia and, consequently, low start-up times and fast dynamic responses.[3,5,6] Furthermore, due to the global reaction exothermicity, it can be performed autothermally, that is, without external heat supply.[2,6] The overall reaction characteristics have turned it a promising technology for decentralized, stationary or onboard, small- to medium-scale applications.[3,4]

Several catalytic formulations have been proposed for performing methane CPOx.[2,7,8] Rh and Pt supported noble metals present the best performances due to its high activity and stability against coke deposition (deactivation).[9,10] Extensive kinetic and mechanistic studies have been performed, in particular for methane CPOx over Rh/Al_2O_3, and several reaction schemes (global and detailed multistep) and kinetic rate expressions have been proposed for a global and elementary chemical description of methane CPOx.[11–13]

Porous heterogeneous catalysts are composed by active metal particles dispersed onto the surfaces of highly porous structures (catalyst carriers/supports—e.g., Al_2O_3, ZrO_2, or SiO_2) in such a way that a high contact area between reactants and active sites is attained per unit of catalyst volume/mass.[14] In packed-bed reactors, porous catalysts can be used directly as catalyst pellets. In structured reactors, porous catalysts are usually applied onto the walls of substrate structures, such as honeycomb or foam monoliths, as a thin layer commonly referred to as the washcoat. Along the complex and tortuous pore structure of porous catalysts some species react and due to the finite rates of mass (and heat) transport, concentration (and temperature) gradients are observed in the catalytic layer. As a consequence, a poorer utilization of precious metals is obtained in relation to that achieved for an infinitely fast transport scenario. Generally, along the pore network of washcoat structures the transport of species is mainly governed by diffusion (advection is negligible).[15–17] Although, depending on the local pore size and operating conditions, different dominant diffusion regimes are observed (molecular or Knudsen diffusion).[18] For modeling purposes, the effect of internal transport limitations on the catalyst performance can be considered implicitly in reaction kinetics (macrokinetics) or through reaction-diffusion models in which intrinsic (transport-free) reaction steps (microkinetics) are treated independently of transport processes.[19]

For solving the reaction-diffusion problem in catalyst porous layers, spatially one-dimensional (1D) to three-dimensional (3D) fully distributed reaction-diffusion

Correspondence concerning this article should be addressed to J. E. P. Navalho at jorge.navalho@tecnico.ulisboa.pt.

mathematical models, considering a pseudohomogeneous (continuum or effective-medium) approach for the pore structure description have been proposed and applied in the literature. The application of 3D models (accounting for simultaneous diffusion and reaction in axial, radial and angular directions) has been less considered because the species diffusion in the washcoat layer along the reactor main flow (axial) direction is largely acknowledged as negligible.[14,20,21] Moreover, for the sake of model performance, 2D models (neglecting axial diffusion) are commonly replaced by 1D models even for a nonuniform washcoat thickness around the honeycomb channel periphery. This approach becomes acceptable for thin washcoat layers.[17] For thick layers, different authors have purposed several strategies to reduce the 2D problem into a 1D approximation.[20,22,23] As the 1D reaction-diffusion problem only has analytical solution for a specific set of requirements that are hardly observed in practice,[14,18] the numerical solution should be addressed or approximations—generalized or simplified effectiveness factors—have to be developed.[21,24,25]

The effect of the catalyst pore structure and metal dispersion/loading on the overall catalyst performance is a relevant issue for the design of improved catalytic reactors. In particular, for hierarchically structured porous catalysts, Coppens and coworkers[26–28] have performed a series of parametric studies with continuum reaction-diffusion models on several morphological parameters (porosity, pore position, pore size, and pore network geometry) to identify optimal structures for different applications. However, due to the simplifying assumptions behind the formulation of continuum models (volume-averaging approach), a meticulous description for all geometrical and topological details of the pore network cannot be expected, particularly considering unsuitable effective transport coefficients. To address this issue, pore-scale (heterogeneous) reaction-diffusion models are increasingly being applied. For monodisperse porous structures, pore-scale diffusion simulations have been performed for determining the overall transport characteristics of electrode porous layers in the fuel cell engineering field.[29] For bidisperse porous media, multiscale methodologies are commonly considered as frameworks for pore-scale diffusion and reaction-diffusion modeling at the different length-scale levels.

In the last few years, several washcoat multiscale diffusion[30–33] and reaction-diffusion[30,32,33] approaches have been developed. In particular, multiscale diffusion (or reaction-diffusion) methods applied to 3D reconstructed porous structures enable the determination of effective transport properties (or average reaction rates) taking into account the pore structure representation, as well as the dominant regimes for species transport at each relevant length-scale level. Through the application of multiscale models, the effect of different structural and catalytic parameters in $Pt/\gamma-Al_2O_3$ coatings for CO oxidation has been extensively investigated at both microscale and macroscale levels.[30,33–35] Multiscale models have also been applied for determining effective transport properties in assemblies of microporous layers—gas diffusion layers[36] and for evaluating the performance of a microstructured methane steam reformer.[32] The application of multiscale models for the evaluation of effective transport coefficients has shown to provide a closer agreement with experimentally measured values than considering the theoretical random pore model.[33,37]

To investigate the effect of internal diffusion limitations on the overall reactor performance, two main upscaling strategies have been suggested for coupling washcoat models (microscale model) with full-scale reactor models (macroscale model): (i) the application of pre-computed look-up tables with average reaction rates – tabulation, mapping, or storage and retrieval approach; and (ii) the direct (iterative) linking between the washcoat model and the full-scale reactor model. The tabulation technique is only readily applied for a priori well-defined operating range and considering kinetic models dependent on a small number of mixture properties.[30,35,38] Conversely, the direct coupling may become extremely computationally demanding, namely for a washcoat 3D multiscale model iteratively called at each macroscale model position (even considering a 1D macroscale model). For this approach, as a compromise between predictability behavior (reliability) and computational workload, less demanding washcoat models are generally preferred. In particular, the direct coupling between a 1D macroscale model and a 1D pseudohomogeneous reaction-diffusion model—the so-called 1D + 1D model—has been largely applied in the literature to account for the washcoat effect on the catalytic combustion of hydrogen[39] and carbon monoxide,[16,40] NO_x storage/reduction and selective catalytic reduction processes,[41,42] and also on the performance of CPOx reactors.[1]

The aim of this work is to develop and apply a multiscale methodology (MSM) capable of transferring the effects of the washcoat pore structure and catalyst conditions from lower length-scales to the full-scale reactor operation. The methodology is applied to investigate the performance of methane catalytic partial oxidation in a honeycomb monolith reactor. For realistic bidisperse porous washcoats, the effect of the internal pore structure on the species transport performance is first addressed. Thereafter, the role of washcoat pore structure and catalyst loading/dispersion is investigated under reactive conditions at the washcoat and full-scale reactor levels. The results from the application of the overall multiscale methodology are compared against those evaluated with a commonly adopted reactor model.

The remainder of this article is organized as follows. The mathematical modeling formulation is presented next, being followed by a section dedicated to the numerical modeling procedures. The succeeding section is devoted to the digital reconstruction of washcoat layers. Thereafter, the results are presented and discussed, and finally, the article ends with summary conclusions.

Mathematical Modeling

The detailed morphological representation of realistic washcoat samples with bimodal pore-size distributions is taken into account on the full-scale reactor model performance with the current multiscale methodology. Figure 1 illustrates the overall multiscale methodology across the three length-scales of interest: nanoscale level (representing the mesopore network structure), microscale level (macropore network structure), and macroscale level (honeycomb channel).

The structure of the microscale level corresponds to a representative section of the washcoat layer that is deposited onto the channel walls of a honeycomb monolith reactor. The physical model of the microscale level consists of a void fraction, with a pore diameter (d_p) range characteristic of macropores ($d_p > 50\,\text{nm}$) and porous microparticles. The internal structure of microparticles is considered in detail at the nanoscale level. At this length-scale level, the microparticle internal structure is described by a cubic representative elementary volume

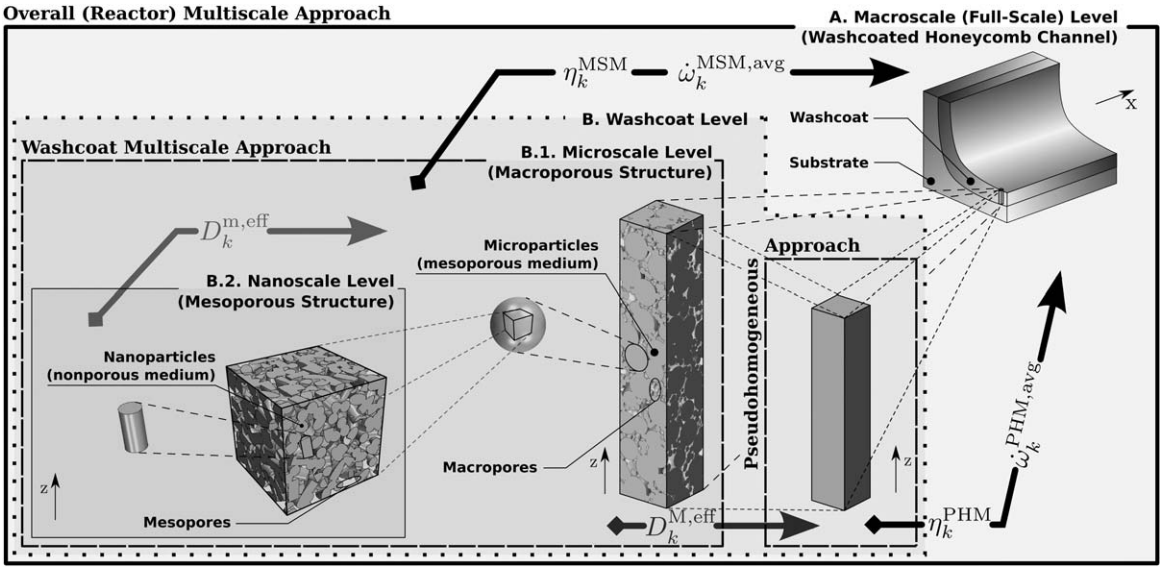

Figure 1. Overall (washcoat and full-scale reactor) multiscale methodology.

composed with solid (nonporous) nanoparticles and mesopores (pores with a diameter range in between 2−50 nm).

The current multiscale methodology is composed by a set of mathematical models developed to embody the relevant phenomena at each length-scale level. These models are coupled in such a way that information gathered at a lower length-scale level is successively transported to the next (upper) length-scale level. Figure 2 shows the models considered in this study, as well as their length-scale range of applicability and the relation between them—hierarchical modeling structure. All models are applied for a steady-state reactor operation. Isothermal conditions are considered on the washcoat modeling formulation. The isothermal washcoat operation is supported by negligible temperature gradients[1,32,43] that are observed due to the typically small washcoat thickness and high effective conductivity.[17,43] The mathematical models and coupling procedures are introduced next.

Washcoat 3D multiscale diffusion and reaction-diffusion models

For the evaluation of washcoat transport properties, 3D pore-scale diffusion simulations are performed sequentially at each washcoat length-scale level, according to a bottom-up approach. Transport coefficients calculated at the nanoscale level are considered as effective values for a pseudohomogeneous species transport description in the microparticles domain at the next modeling level—microscale level. At the microscale level, a similar averaging procedure of that conducted at the nanoscale level is performed to extract overall effective diffusivity values along the whole bidisperse porous

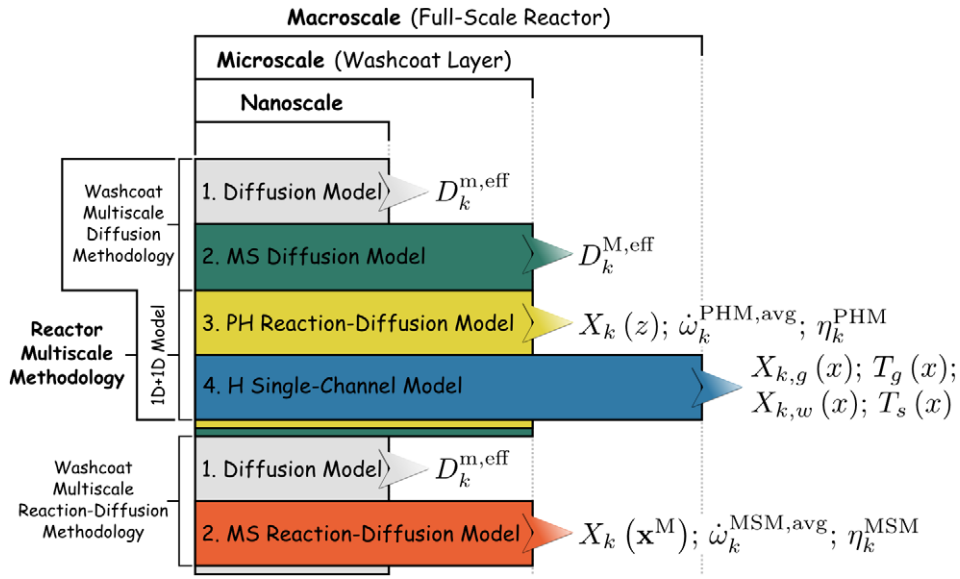

Figure 2. Multiscale methodology: models, range of applicability, and hierarchical structure. MS – multiscale; PH – pseudohomogeneous; H – heterogeneous.

[Color figure can be viewed at wileyonlinelibrary.com]

layer. Under reactive conditions, the role of the mesoporous and macroporous structures and catalyst distribution (loading and dispersion) on the overall washcoat performance (average reaction rates) is considered through the application of the diffusion model at the nanoscale level, and the reaction-diffusion model at the microscale level—see the hierarchical structure of the washcoat multiscale reaction-diffusion methodology in Figure 2.

Nanoscale diffusion model. The diffusion of species in the 3D mesopore domain is mathematically described through Eq. 1, considering that at this length-scale level the continuum approach is an acceptable assumption.[44] In Eq. 1, c corresponds to the mixture molar concentration (evaluated with the ideal gas law), D_k^{m} to the (local) species diffusion coefficients, and X_k to the mole fraction of species k

$$\nabla.\left(cD_k^{\mathrm{m}}\nabla X_k\right)=0 \tag{1}$$

At the nanoscale level, due to the small pore sizes, molecules collide more often with the pore walls than with themselves and for that reason, the species transport becomes primarily governed by Knudsen diffusion than by the molecular diffusion regime. Therefore, the species diffusion coefficients required in Eq. 1 are calculated with Eq. 2 (Knudsen diffusivity equation), where $r_p\left(\mathbf{x}^{\mathrm{m}}\right)$ is the pore radius at the location $\mathbf{x}^{\mathrm{m}}$ of the mesopore space and R, T, and W_k correspond to the ideal gas constant, temperature, and molecular weight of species k, respectively

$$D_{k,\mathrm{K}}=\frac{2}{3}r_p\left(\mathbf{x}^{\mathrm{m}}\right)\sqrt{\frac{8RT}{\pi W_k}} \tag{2}$$

A dominant direction for species transfer in the mesopore network is imposed through the application of proper boundary conditions. Eq. 1 is subjected to Dirichlet boundary conditions on the two opposed (parallel) z-direction boundaries of the computational domain, while zero-diffusive molar fluxes (homogeneous Neumann boundary conditions) are considered on the remaining four boundaries.

After a converged solution is achieved for the species concentration fields, the average diffusive molar flux for each species along the dominant mass-transfer direction is evaluated through Eq. 3, where $V_T^{\mathrm{m}}\left(=\delta_x^{\mathrm{m}}\times\delta_y^{\mathrm{m}}\times\delta_z^{\mathrm{m}}\right)$ corresponds to the total volume of the mesoporous structure representative elementary volume and V_p^{m} corresponds to the total mesopore (void) volume

$$J_k^{\mathrm{m,avg}}=\frac{1}{V_T^{\mathrm{m}}}\int_{V_p^{\mathrm{m}}}-cD_k^{\mathrm{m}}\frac{\partial X_k}{\partial z}dV \tag{3}$$

Finally, the effective diffusion coefficients for each species at the nanoscale level are computed with Eq. 4 that corresponds to the Fick's first law of diffusion considering a molar flux applied to a pseudohomogeneous planar medium with constant (effective) diffusivity. In Eq. 4, $c\left(X_k^1-X_k^0\right)$ is the concentration difference imposed by the boundary conditions and δ_z^{m} corresponds to the thickness of the mesoporous sample in the z-direction (dominant mass-transfer direction)

$$D_k^{\mathrm{m,eff}}=-J_k^{\mathrm{m,avg}}\frac{\delta_z^{\mathrm{m}}}{c\left(X_k^1-X_k^0\right)} \tag{4}$$

Microscale diffusion and reaction-diffusion models. The governing equation of the microscale diffusion model corresponds to the steady-state formulation of Fick's second law (Eq. 1). The species diffusion coefficients for the microscale diffusion mathematical model (D_k^{M}) can take two different values depending on the local position in the microscale physical model ($\mathbf{x}^{\mathrm{M}}$), as Eq. 5 presents. In macropores, molecular diffusion prevails over Knudsen diffusion as the molecular mean free path is typically much smaller than the pore sizes. In Eq. 5, $D_{k,\mathrm{b}}$ corresponds to the species bulk diffusion coefficients and $D_k^{\mathrm{m,eff}}$ to the species effective (spatially independent) diffusion coefficients in the mesoporous microparticles (evaluated through the nanoscale diffusion model)

$$D_k^{\mathrm{M}}\left(\mathbf{x}^{\mathrm{M}}\right)=\begin{cases}D_{k,\mathrm{b}} & \text{if } \mathbf{x}^{\mathrm{M}}\in \text{ Macropore space}\\ D_k^{\mathrm{m,eff}} & \text{if } \mathbf{x}^{\mathrm{M}}\notin \text{ Macropore space}\end{cases} \tag{5}$$

The molecular diffusion coefficients are computed with the correlation[45] presented in Eq. 6, considering multicomponent diffusion coefficients approximated by binary diffusion coefficients for each species in a bath mixture of N_2

$$D_{k,\mathrm{b}}=\frac{0.00143T^{1.75}}{P\sqrt{2/\left(1/W_k+1/W_{\mathrm{N_2}}\right)}\left[\left(\Sigma_v\right)_k^{1/3}+\left(\Sigma_v\right)_{\mathrm{N_2}}^{1/3}\right]^2} \tag{6}$$

The same set of boundary conditions employed for the nanoscale diffusion model is applied for the microscale diffusion model. For calculating the overall (microscale) effective diffusion coefficients ($D_k^{\mathrm{M,eff}}$), a similar procedure of that presented for the nanoscale model is considered.

Under reacting conditions, the evaluation of the washcoat layer performance is performed with Eq. 7 that corresponds to the governing equation of the microscale reaction-diffusion model. The local diffusion coefficients required in Eq. 7 are determined according to Eq. 5

$$\nabla.\left(cD_k^{\mathrm{M}}\nabla X_k\right)+\dot{\omega}_k^{\mathrm{MSM}}=0 \tag{7}$$

In Eq. 7, $\dot{\omega}_k^{\mathrm{MSM}}$ corresponds to the species molar production/destruction rates on a volume basis due to surface reactions. According to Eq. 8, surface reactions are only accounted for in the microparticles' domain (mesoporous structure). In this equation, $\dot{s}_k$ corresponds to the species net production rates on an active surface basis, $F_{\mathrm{cat/geo}}^{\mathrm{m}}$ denotes the ratio between the catalytic active surface area and the geometrical surface area of the mesoporous structure, and a_V^{m} is the geometrical surface area per unit volume of the mesoporous structure

$$\dot{\omega}_k^{\mathrm{MSM}}\left(\mathbf{x}^{\mathrm{M}}\right)=\begin{cases}0 & \text{if } \mathbf{x}^{\mathrm{M}}\in \text{ Macropore space}\\ \dot{s}_k\left(\mathbf{x}^{\mathrm{M}}\right)F_{\mathrm{cat/geo}}^{\mathrm{m}}a_V^{\mathrm{m}} & \text{if } \mathbf{x}^{\mathrm{M}}\notin \text{ Macropore space}\end{cases} \tag{8}$$

For each species, Eq. 7 is subjected to zero-flux boundary conditions in the x- and y-directions, and on the surface $z=0$—interface between the washcoat layer and the monolith support structure (substrate). A Dirichlet boundary condition is imposed on the microscale structure top-surface ($z=\delta_z^{\mathrm{M}}$) to represent the mixture composition at the external washcoat surface.

The solution of the microscale reaction-diffusion model is applied for the determination of spatially averaged species net production rates through Eq. 9, where $V_T^{\mathrm{M}}\left(=\delta_x^{\mathrm{M}}\times\delta_y^{\mathrm{M}}\times\delta_z^{\mathrm{M}}\right)$ corresponds to the total volume of the microscale physical model

$$\dot{\omega}_k^{\mathrm{MSM,avg}}=\frac{1}{V_T^{\mathrm{M}}}\int_{V_T^{\mathrm{M}}}\dot{\omega}_k^{\mathrm{MSM}}\left(\mathbf{x}^{\mathrm{M}}\right)dV \tag{9}$$

For determining the extent of internal diffusion resistances in a specific washcoat layer, the internal effectiveness factor for the creation/depletion rates of each reacting species is calculated according to Eq. 10, where ϵ^{M} is the porosity of the

microscale (macroporous) structure and $\dot{\omega}_k^{\mathrm{MSM,bnd}}$ corresponds to the species net production rates evaluated with Eq. 8 at a position $\mathbf{x}^{\mathrm{M}}=\left(x,y,\delta_z^{\mathrm{M}}\right)$ belonging to the microparticles' domain

$$\eta_k^{\mathrm{MSM}}=\frac{1}{\left(1-\epsilon^{\mathrm{M}}\right)}\frac{\dot{\omega}_k^{\mathrm{MSM,avg}}}{\dot{\omega}_k^{\mathrm{MSM,bnd}}} \tag{10}$$

Washcoat 1D pseudohomogeneous reaction-diffusion model

The 1D pseudohomogeneous reaction-diffusion model (PHM) considers species transport only along the washcoat thickness (z-direction), as stated in Eq. 11

$$\frac{d}{dz}\left(cD_k^{\mathrm{M,eff}}\frac{dX_k}{dz}\right)+\dot{\omega}_k^{\mathrm{PHM}}=0 \tag{11}$$

According to a recent study,[33] the predictive capability of this model is significantly improved by providing effective transport properties evaluated through the application of multiscale diffusion models. Therefore, the effective diffusion coefficients required in Eq. 11 are calculated through the washcoat multiscale diffusion model rather than being computed with unsuitable semitheoretical correlations. The species source term is given by Eq. 12, where $a_V^{\mathrm{M,T}}\left(=a_V^{\mathrm{m}}\left(1-\epsilon^{\mathrm{M}}\right)\right)$ denotes the total specific surface area of the bimodal porous structure. The product $F_{\mathrm{cat/geo}}^{\mathrm{m}}a_V^{\mathrm{M,T}}$ corresponds to the total catalytic surface area per unit volume at the microscale level—$a_{V,\mathrm{cat}}^{\mathrm{M,T}}$

$$\dot{\omega}_k^{\mathrm{PHM}}(z)=\dot{s}_k(z)F_{\mathrm{cat/geo}}^{\mathrm{m}}a_V^{\mathrm{M,T}} \tag{12}$$

Equation 11 is subjected to the same set of boundary conditions as the microscale reaction-diffusion governing equation (Eq. 7) in the z-direction. Once a converged solution for the species concentration fields is obtained, the species average production/destruction rates and the species effectiveness factors can be determined through Eqs. 13 and 14, respectively

$$\dot{\omega}_k^{\mathrm{PHM,avg}}=\frac{1}{\delta_z^{\mathrm{M}}}\int_0^{\delta_z^{\mathrm{M}}}\dot{\omega}_k^{\mathrm{PHM}}(z)dz \tag{13}$$

$$\eta_k^{\mathrm{PHM}}=\frac{\dot{\omega}_k^{\mathrm{PHM,avg}}}{\dot{\omega}_k^{\mathrm{PHM,bnd}}} \tag{14}$$

Reactor 1D heterogeneous single-channel model

The current 1D heterogeneous single-channel mathematical model has been widely applied in the literature to predict the overall (full-scale) performance of monolith reactors.[46,47] The model is composed by mass balance equations for the bulk gas species (Eq. 15) and for the species at the interface between the external gas flow and the washcoat surface (Eq. 17), and by energy balance equations for the gas and solid phases (Eqs. 16 and 18, respectively). Ordinary molecular diffusion and thermal diffusion (Soret effect) are considered in Eq. 15. The correction velocity approach[48] is used to ensure the total mass conservation. A negligible homogeneous (gas-phase) conversion path for reactants and surface reaction products is widely acknowledged during methane catalytic partial oxidation at atmospheric pressure and typical contact times.[49] Thermal radiation is accounted for in the solid phase through the application of the zone method[50]

$$A\epsilon^{\mathrm{F}}\rho_g u\frac{dY_{k,g}}{dx}+\frac{d}{dx}\left(A\epsilon^{\mathrm{F}}\rho_g Y_{k,g}V_{k,g}\right)+Aa_V^{\mathrm{F}}\rho_g K_{\mathrm{mat},k}\left(Y_{k,g}-Y_{k,w}\right)=0 \tag{15}$$

$$A\epsilon^{\mathrm{F}}\rho_g uC_{p,g}\frac{dT_g}{dx}-\frac{d}{dx}\left(A\epsilon^{\mathrm{F}}k_g\frac{dT_g}{dx}\right)+A\epsilon^{\mathrm{F}}\rho_g\sum_{k=1}^{K_g}Y_{k,g}V_{k,g}C_{p,k}\frac{dT_g}{dx}+Aa_V^{\mathrm{F}}h\left(T_g-T_s\right)=0 \tag{16}$$

$$a_V^{\mathrm{F}}\rho_g K_{\mathrm{mat},k}\left(Y_{k,g}-Y_{k,w}\right)+a_V^{\mathrm{F}}\dot{\omega}_k^{\mathrm{F}}W_k=0 \tag{17}$$

$$-\frac{d}{dx}\left(Ak_{s,\mathrm{eff}}\frac{dT_s}{dx}\right)-Aa_V^{\mathrm{F}}h\left(T_g-T_s\right)+Aa_V^{\mathrm{F}}\sum_{k=1}^{K_g}\dot{\omega}_k^{\mathrm{F}}H_k+Aa_V^{\mathrm{F}}q_{\mathrm{rad}}''=0 \tag{18}$$

In Eqs. 15–18, A is the reactor cross-sectional area, ϵ^{F} is the (full-scale) reactor porosity, ρ_g is the bulk gas mass density, $V_{k,g}$ is the species diffusion velocities, a_V^{F} is the reactor specific surface area, and q_{rad}'' is the net radiative heat flux from the solid phase. $Y_{k,g}$ ($Y_{k,w}$) and T_g (T_s) correspond to the species mass fractions in the bulk gas (wall) mixture, and to the gas (solid) temperature, respectively.

As the model under consideration is simultaneously a two-phase model and a lumped model in the radial and angular directions, heat and mass convection (interphase transport) between the bulk gas flow and the washcoat external surface is accounted for through proper Nusselt and Sherwood number correlations. In this work, the interphase heat transfer coefficient (h) is determined through the local Nusselt number correlation given by Eq. 19, that is suited for square-shaped channels under laminar flow conditions.[51] In Eq. 19, $(x-x_{\mathrm{in}})$ corresponds to the distance from the inlet section (to account for entrance effects), d_h is the channel hydraulic diameter, and Pe_{T} is the thermal Péclet number. The interphase species mass-transfer coefficients ($K_{\mathrm{mat},k}$) are determined through the local Sherwood number correlation derived from the application of the Chilton-Colburn analogy to Eq. 19

$$Nu(x)=2.977+8.827\left[1000\left(\frac{x-x_{\mathrm{in}}}{d_hPe_{\mathrm{T}}}\right)\right]^{-0.545}\mathrm{Exp}\left[-48.2\left(\frac{x-x_{\mathrm{in}}}{d_hPe_{\mathrm{T}}}\right)\right] \tag{19}$$

The species molar production/destruction rates ($\dot{\omega}_k^{\mathrm{F}}$) are calculated differently depending on whether or not mass transfer limitations in the washcoat layer are considered, as Eq. 20 states

$$\dot{\omega}_k^{\mathrm{F}}(x)=\begin{cases}\dot{\omega}_k^{\mathrm{PHM,avg}}(x)\delta_z^{\mathrm{M}} & \text{1D+1D model}\\ \dot{s}_k(x)F_{\mathrm{cat/geo}}^{\mathrm{m}}a_V^{\mathrm{m}}\left(1-\epsilon^{\mathrm{M}}\right)\delta_z^{\mathrm{M}} & \text{Instantaneous diffusion approach − 1D model}\end{cases} \tag{20}$$

According to this equation, internal diffusion limitations are embodied in the full-scale reactor model through the 1D + 1D model approach: for each reactor axial position (x), the macroscale model provides the wall mixture composition ($Y_{1,w},\ldots,Y_{K_g,w}$), temperature (T_s), and pressure to the 1D PHM; thereafter, this washcoat model returns to the

macroscale model the species average production/depletion rates in the washcoat layer ($\dot{\omega}_k^{\mathrm{PHM,avg}}$) computed with Eq. 13. Equation 20 also presents the expression to compute $\dot{\omega}_k^{\mathrm{F}}$ if the same amount of catalyst were readily available without transport limitations (1D+0D reactor model—shortly 1D model). In Eq. 20, the washcoat thickness (δ_z^{M}) stems from the assumption of a slab washcoat geometry. The product $F_{\mathrm{cat/geo}}^{\mathrm{m}} a_V^{\mathrm{m}} (1-\epsilon^{\mathrm{M}})\delta_z^{\mathrm{M}}$ corresponds to the ratio of catalytic surface area to geometric surface area evaluated at the macroscale level—$F_{\mathrm{cat/geo}}^{\mathrm{F}}$. Experimentally, this ratio can be calculated with Eq. 21 taking into account the catalyst loading (m_{Rh}) and metal dispersion (D_{Rh}) on the evaluation of the total catalytic surface area ($\mathrm{A}_{\mathrm{cat}}^{\mathrm{M,T}}$)

$$F_{\mathrm{cat/geo}}^{\mathrm{F}} = \frac{A_{\mathrm{cat}}^{\mathrm{M,T}}}{A_{\mathrm{geo}}^{\mathrm{F}}} = D_{\mathrm{Rh}} \frac{m_{\mathrm{Rh}}}{W_{\mathrm{Rh}}} \frac{1}{\Gamma} \frac{1}{A_{\mathrm{geo}}^{\mathrm{F}}} \tag{21}$$

The gas phase balance equations (Eqs. 15 and 16) are subjected to Danckwerts boundary conditions. The solid energy balance equation (Eq. 18) is subjected to radiative boundary conditions.

Surface chemistry model

The species molar production/destruction rates on an active surface basis are determined with Eq. 22, where I corresponds to the total number of reactions, k_i is the rate coefficient of each reaction, and K_g (K_s) is the total number of gas phase (surface—adsorbed) species

$$\dot{s}_k = \sum_{i=1}^{I} \nu_{ki} \left(k_i \prod_{k=1}^{K_g+K_s} c_k^{\nu'_{ki}} \right) \tag{22}$$

The rate coefficient for adsorption reactions is calculated through Eq. 23, where γ_i corresponds to the sticking coefficient, Γ to the surface site density, and the exponent τ is the sum of stoichiometric coefficients of surface reactants. For surface and desorption reactions, the rate coefficient is computed with Eq. 24, where the coverage parameters μ_{ki} and ϵ_{ki} are introduced to modify the pre-exponential factor (A_i) and activation energy (E_i), respectively, to account for different binding states depending on the actual surface coverage

$$k_i = \frac{\gamma_i}{\Gamma^{\tau}} \sqrt{\frac{RT_s}{2\pi W_k}} \tag{23}$$

$$k_i = A_i T_s^{\beta_i} \mathrm{Exp}\left(\frac{-E_i}{RT_s}\right) \prod_{k=1}^{K_s} \theta_k^{\mu_{ki}} \mathrm{Exp}\left(\frac{\epsilon_{ki}\theta_k}{RT_s}\right) \tag{24}$$

Species surface coverages ($\theta_1, \ldots, \theta_{K_s}$) are determined through the solution of Eq. 25. At steady-state, this equation implies equal rates for surface species production and depletion ($\dot{s}_k = 0$)

$$\frac{d\theta_k}{dt} = \frac{\dot{s}_k \sigma_k}{\Gamma} \tag{25}$$

For describing the partial oxidation of methane on $\mathrm{Rh}/\mathrm{Al_2O_3}$ catalysts, the improved multistep reaction mechanism recently developed by Deutschmann and coworkers[52] is herein considered. The reaction mechanism comprises 48 elementary and irreversible reaction steps, involving 6 gas phase species, and 12 surface species. The surface site density was set equal to 2.72×10^{-9} mol.cm^{-2} in agreement with the literature.[49,52]

Numerical Modeling

The washcoat 3D multiscale diffusion and reaction-diffusion models were numerically solved through the commercial software STAR-CCM+. CAD modeling and mesh generation were also performed within the STAR-CCM+ package. The suitable mesh for each case was determined according to preliminary mesh independence studies on the final model solution. The gas mixture was considered as a multicomponent ideal gas mixture at isothermal and steady-state conditions. The species mass-balance equations were solved through the built-in segregated species model, according to which the governing equations are solved sequentially for all species but one (diluting species) whose solution is computed to guarantee the overall mass conservation. Surface chemical kinetics (surface chemistry model) was accounted for in the commercial code through externally coded user libraries. These libraries were developed to calculate the species production/destruction rates considering the local mixture composition, temperature, and pressure and the microparticles' internal active surface area per unit volume. The kinetic interpreter provided in the CANTERA object-oriented suite[53] was coupled to the user libraries for solving the governing equation of species surface coverages. The multiscale diffusion and reaction-diffusion methodologies and underlying models solved according to the current numerical procedure have been successfully validated in the past.[33,35]

In-house versions of the PREMIX code[54] were developed to solve the 1D PHM (for the prediction of the continuum washcoat layer performance) and the 1D heterogeneous single-channel model (for the description of the full-scale reactor operation). For all 1D model applications, a mesh with sufficient grid points to ensure a mesh-independent solution was regarded. The 1D heterogeneous full-scale reactor model has been extensively validated for methane CPOx.[46,50]

Washcoat Structure Reconstruction

The morphology of a fresh washcoat porous structure depends on the base material used and on the preparation procedures. Furthermore, depending on the length-scale considered, the existence of different particle shapes and characteristic particle sizes can be perceived through high-resolution imaging techniques. In particular, for $\gamma-\mathrm{Al_2O_3}$ porous layers, scanning electron microscopy (SEM) images reveal that the grains composing the macroporous structure (microparticles—see Figure 1) can be approximated as spherical particles.[30,37] However, at a nanoscale level, transmission electron microscopy (TEM) images suggest that the structural primary particles (nanoparticles—see Figure 1) have a cylinder-shaped geometry.[30]

The virtual generation of macroporous/mesoporous structures is herein performed numerically, through a particle packing code[55] that takes into consideration experimental parameters evaluated with realistic catalyst porous layers, viz. porosity, particle shape, and particle-size distribution. At the end of the reconstruction process, the computer-generated structure is represented by a 3D discrete volume phase function addressing for each voxel the corresponding space (solid or void).

In this work, three different mesoporous structures and three different macroporous structures were reconstructed. The three mesoporous structures (designated by $\mathrm{S_a}$, $\mathrm{S_b}$, and $\mathrm{S_c}$) were generated considering cylinder-shaped grains as primary particles—characterized by its diameter (d_c^{m}) and length (l_c^{m})—

Table 1. Properties of the Three Virtually Reconstructed Mesoporous Structures

	Mesoporous Structure		
Structural/Geometrical Parameter	S_a	S_b	S_c
Cylinder length—l_c^m [nm]	20	20	20
Cylinder diameter—d_c^m [nm]	10	10	10
Porosity—ϵ^m [−]	0.29	0.43	0.63
System size—$\delta_x^m \times \delta_y^m \times \delta_z^m$ [nm^3]	100×100×100	100×100×100	100×100×100
Specific surface area – a_V^m [nm^{-1}]	0.226	0.222	0.164

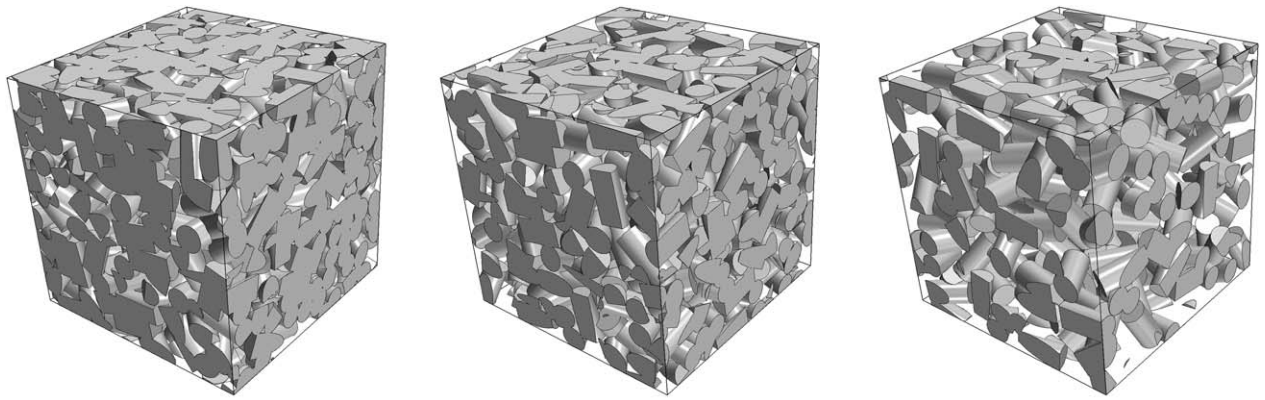

Figure 3. Computer-reconstructed mesoporous structures: (a) mesoporous structure S_a; (b) mesoporous structure S_b; (c) mesoporous structure S_c.

along with the structural/geometrical parameters listed in Table 1. Among the required parameters for media generation, only the mesoporosity (ϵ^m) is varied. A cubic system (representative elementary volume) with 1.0×10^6 nm^3 is considered for all mesoporous samples. The specific surface area presented in Table 1 was evaluated after the reconstruction procedure.

Figure 3 shows the three mesoporous structures composed by packings of cylinder-shaped nanoparticles. An increase in the porosity is evident from the structure S_a to the structure S_c. As the nanoparticles are nonporous (impermeable), the void volume of each mesoporous structure corresponds to the actual computational domain for the nanoscale diffusion model.

The three macroporous structures (labeled as S_A, S_B, and S_C) were developed considering spheres as primary particles. Table 2 presents the structural/geometrical parameters required for the generation of each macroporous structure. Two particle sizes ($d_{s_1}^M$ and $d_{s_2}^M$) are considered along with a specific mixing ratio (s_1/s_2). The difference between each set of parameters required for the reconstruction of these structures relies only on the macroporosity (ϵ^M). The macroporous samples—sections of washcoat layers (see Figure 1)—have a constant thickness of 50 μm.

To further characterize the generated structures, the pore-size distribution of each sample was evaluated through the maximum sphere inscription method[44] and is presented in Figures 4a and 4b for the mesoporous and macroporous structures, respectively. As the mesoporosity/macroporosity is increased, the sample pore size range becomes wider and the mean pore diameter ($\overline{d_p}$) increases—from 5.795, 8.151 to 14.253 nm for the mesoporous structures S_a, S_b, and S_c, respectively, and from 0.516, 0.969 to 1.491 μm for the macroporous structures S_A, S_B, and S_C, respectively. The geometrical parameters, porosity, and pore-size ranges for the digitally reconstructed porous samples are within typical experimental values reported in the literature for similar porous structures.[30,56]

Results and Discussion

The reforming reactor is composed by a 1.5 cm long inert heat shield placed in front of a 3.0 cm long catalyst block. The heat shield and the catalyst have an external diameter equal to 2.5 cm and are made up of 600 cpsi cordierite honeycomb monoliths with square-shaped cells. The heat shield and the catalyst honeycomb after washcoat deposition have a total porosity equal to 70%.

Table 2. Properties of the Three Virtually Reconstructed Macroporous Structures

	Macroporous Structure		
Structural/Geometrical Parameter	S_A	S_B	S_C
Sphere 1 diameter—$d_{s_1}^M$ [μm]	5.0	5.0	5.0
Sphere 2 diameter—$d_{s_2}^M$ [μm]	1.2	1.2	1.2
Mixing ratio—s_1/s_2 [−]	1/16	1/16	1/16
Porosity—ϵ^M [−]	0.05	0.18	0.30
System size—$\delta_x^M \times \delta_y^M \times \delta_z^M$ [μm^3]	10×10×50	10×10×50	10×10×50
Specific surface area—a_V^M [μm^{-1}]	0.619	0.907	0.869

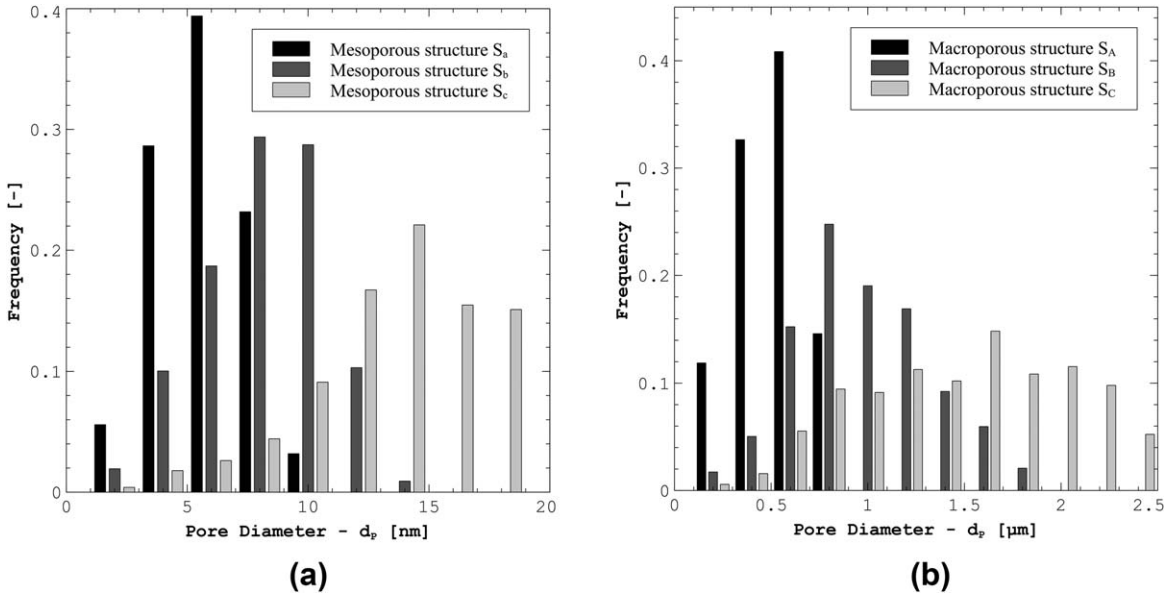

Figure 4. Pore-size distributions for the generated porous media: (a) mesoporous structures; (b) macroporous structures.

The three mesoporous structures (S_x) and the three macroporous structures (S_X) previously developed are herein combined together to assemble a total of nine different bimodal porous layers (S_{x-X}). Different active surface areas for each structure are considered as well. Therefore, each catalytic washcoat sample is identified as $S_{x-X}^{F_{cat/geo}^F}$, where the $F_{cat/geo}^F$ value defines the actual catalyst loading/dispersion applied onto the pore walls of the inactive combined (bidisperse) structure S_{x-X}. For typical Rh/Al_2O_3 washcoat layers, experimental $F_{cat/geo}^F$ values ranging from 5.0 to 30.0 are well-supported by the literature.[21,57,58]

In the current work, numerical simulations are conducted at steady-state conditions and under atmospheric pressure. At the macroscale level, the reactor is fed with a gas mixture preheated to 400 K of methane and air, with an air-to-fuel equivalence ratio of 0.30 (molar O/C ratio equal to 1.2). A total mass flow rate equal to $0.19\,g.s^{-1}$ (ca. $10\,NL.min^{-1}$) is considered.

The results and discussion are organized in three subsections. In the first subsection, the effect of different mesopore/macropore network morphologies is presented in terms of mass transport properties. Thereafter, under reacting conditions the role of pore structure and catalytic surface area is investigated on: (1) the washcoat performance (second subsection); and (2) the full-scale reactor performance at short-contact time methane partial oxidation conditions (third subsection).

Effect of washcoat pore structure on species transport

Pore-scale diffusion simulations performed at the nanoscale level for a temperature equal to 298.15 K revealed the following CH_4 effective diffusion coefficients ($D_{CH_4}^{m,eff}(298.15\,K)$) in the mesoporous structures S_a, S_b, and S_c: 1.025, 3.528, and $12.420 \times 10^{-7}\ m^2.s^{-1}$, respectively. Effective transport coefficients increase with the mesoporosity (and mean pore radius) values. For each species at a constant temperature, the effective diffusion coefficients in the samples S_b and S_c are about 3.4 and 12.1, respectively, higher than the effective diffusion coefficient in the sample S_a. The results were evaluated considering polyhedral meshes (to provide a high geometrical fidelity) with about 1.7, 1.6, and 1.3 million cells for the structures S_a, S_b, and S_c, respectively. The computed effective diffusion coefficients are within typical values for mesoporous structures.[30,33]

Figure 5a presents the overall CH_4 effective diffusion coefficients along the temperature range 900–1300 K for the nine mesoporous–macroporous structural combinations considered. A trimmed mesh with about 1.5 million hexahedral cells was considered for solving the washcoat 3D multiscale models at the microscale level. Regardless the temperature, Figure 5a shows that the structures S_{a-A} and S_{c-C} present the minimum and maximum CH_4 effective diffusion coefficients, respectively. The range of effective diffusivity values calculated for all structures is in agreement with usual values reported in the literature.[30,56] The increasing trend with temperature presented by the effective diffusion coefficients for CH_4 (and for the remaining species—not shown) depends on the structure, mainly on the macroporous structure. As the macropore void fraction increases, the dependence on temperature observed for the CH_4 effective diffusion coefficients becomes closer to the temperature dependence considered for computing the transport coefficients in a pure molecular diffusion regime (see Eq. 6).

For the nine combined structures at a constant temperature, Figure 5b presents the effective diffusion coefficients for all reactive gas species, as well as the ratios between the effective diffusion coefficients of CH_4 and the remaining reactive species, that is, $D_{CH_4}^{M,eff}/D_j^{M,eff}$—effective diffusivity ratios. For all combined structures, H_2 and CO_2 present the highest and lowest values for effective diffusivities, respectively. The effect of the actual mesoporous structure on the species effective diffusion coefficients becomes less relevant as the macroporosity increases. The effective diffusivity ratios ($D_{CH_4}^{M,eff}/D_j^{M,eff}$) at a constant temperature and pressure are dependent on the combined structure under consideration. This evidence is consistent with the contribution of two different (competing) regimes of diffusion—Knudsen and molecular regimes—on the effective diffusion coefficients. As the macroporosity increases (or the mesoporosity decreases), the effective diffusivity ratios tend to approach the ratio $D_{CH_4,b}/D_{j,b}$ that is obtained in the absence of a Knudsen diffusive transport

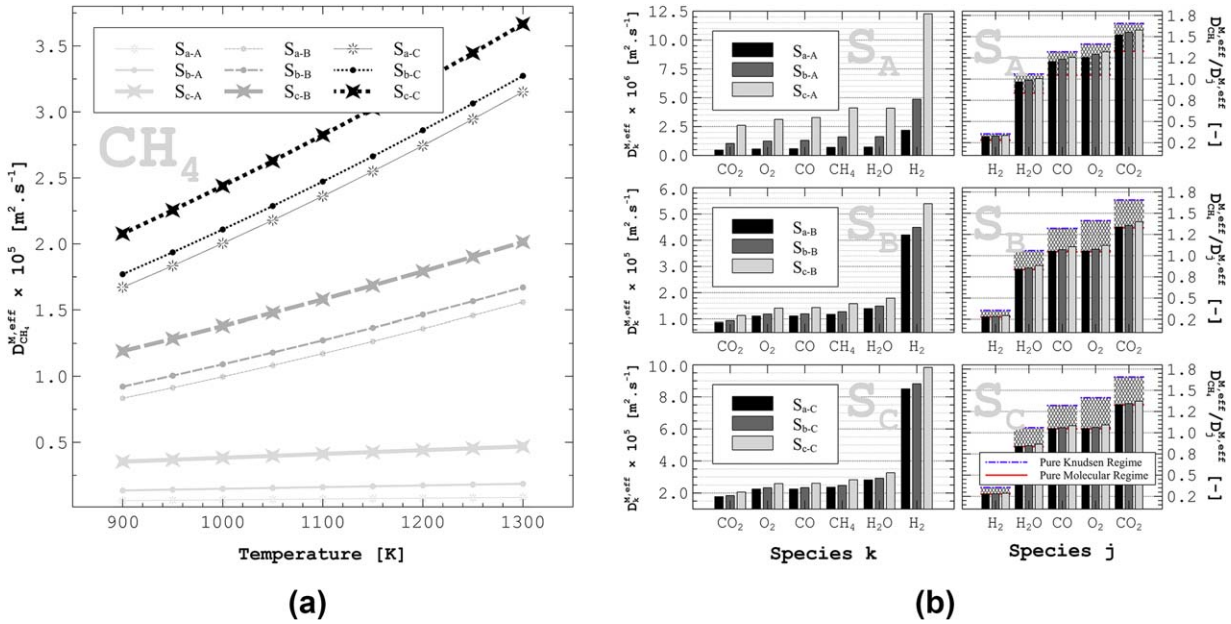

Figure 5. Overall effective diffusion coefficients in the nine porous structures at 1 atm: (a) for CH_4 over the temperature range 900−1300 K; (b) for all reactive species (including the effective diffusivity ratios between different species) at the temperature of 1100 K.

[Color figure can be viewed at wileyonlinelibrary.com]

regime—lower bound of the shaded intervals in Figure 5b. Conversely, decreasing the macroporosity (or increasing the mesoporosity) leads progressively the effective diffusivity ratios toward the value $\sqrt{W_j/W_{CH_4}}$, which is attained in the limiting scenario of a sample composed exclusively by mesopores—upper bound of the shaded intervals in Figure 5b.

The influence of the mesoporosity/macroporosity on the overall effective diffusivity values (and ratios) can be justified on the basis of the relative importance of diffusion along microparticles evaluated through Eq. 26. Figure 6a presents the relative importance of CH_4 diffusion along mesopores for all combined structures at a constant temperature, whereas Figure 6b presents the relative importance of diffusion in microparticles for all reactive species in the structures $S_{c–A}$ and $S_{a–C}$ along the temperature range of 900–1300 K

$$\xi_k\,[\%] = \frac{\int_{V_T^M - V_p^M} D_k^{m,eff}\,\frac{\partial X_k}{\partial z}\,dV}{\int_{V_T^M} D_k^M(\mathbf{x}^M)\,\frac{\partial X_k}{\partial z}\,dV} \times 100\% \tag{26}$$

Figure 6a reveals that an increase in the macroporosity (or a decrease in the mesoporosity) reduces the weight of a Knudsen-controlled regime (species transport in

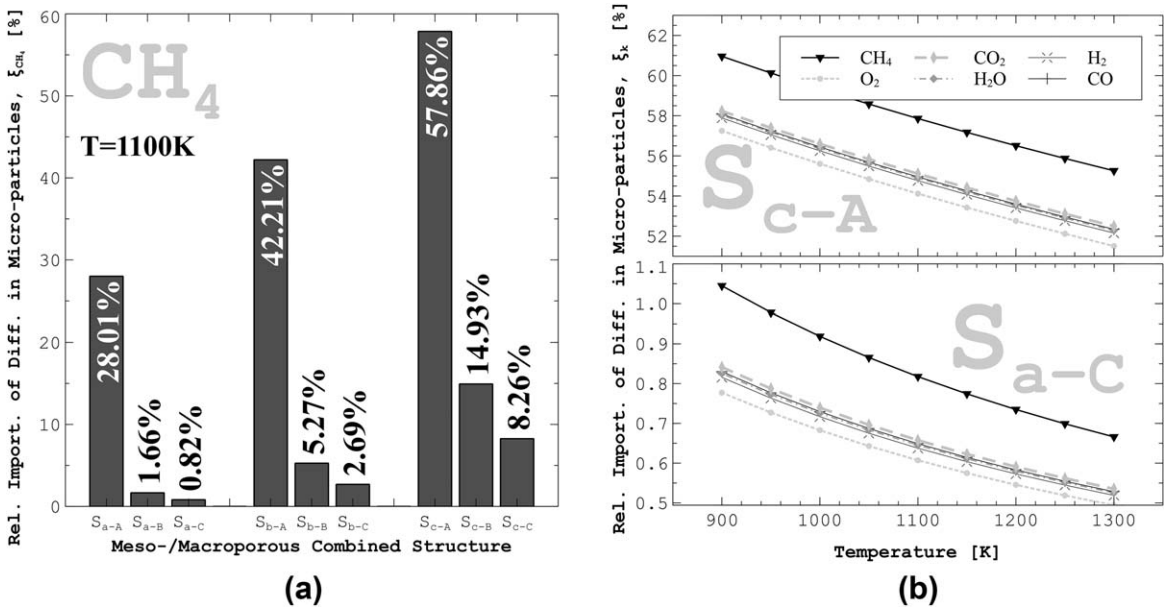

Figure 6. Relative importance of diffusion in mesoporous microparticles at 1 atm: (a) for methane in all structures at 1100 K; (b) for every reactive species in the structures $S_{c–A}$ and $S_{a–C}$ over the temperature range 900−1300 K.

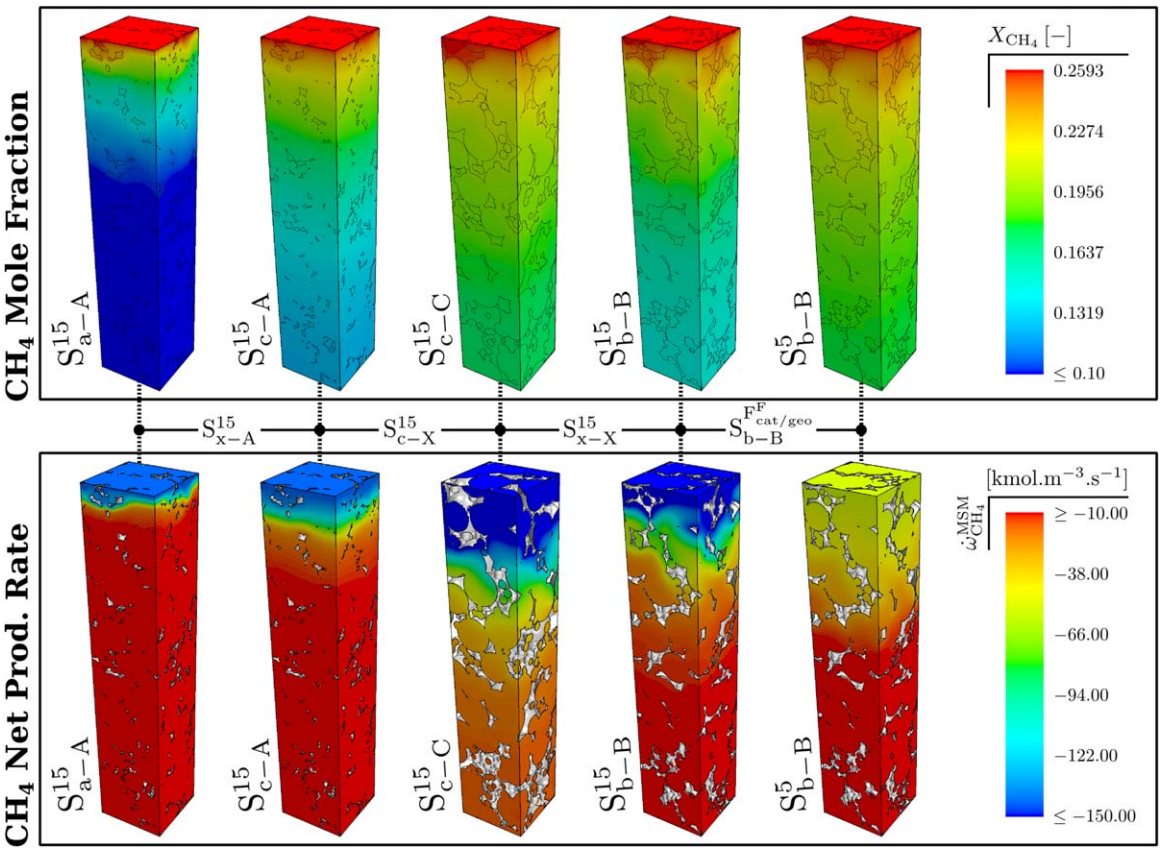

Figure 7. 3D multiscale reaction-diffusion model results for the structures S^{15}_{a-A}, S^{15}_{c-A}, S^{15}_{c-C}, S^{15}_{b-B}, and S^{5}_{b-B}: CH_4 mole fraction (upper row) and CH_4 net production rate (lower row).

[Color figure can be viewed at wileyonlinelibrary.com]

microparticles) on the overall effective diffusion coefficient. Consequently, species transport becomes increasingly dominated by a molecular diffusion regime (through macropores). The effective diffusivity ratios (see Figure 5b) decrease as the relative importance of diffusion in microparticles decreases. Figure 6b shows that apart from the structure and temperature under consideration, CH_4 and O_2 are the species featuring the highest and lowest transport contribution from microparticles on the overall transport coefficient, respectively. For any combined structure, the relative importance of species transport in microparticles decreases with temperature because the less resistive molecular transport regime in macropores is promoted over the species transport in mesopores (see the temperature dependence on $D_{k,\mathrm{K}}$ and $D_{k,\mathrm{b}}$—Eqs. 2 and 6, respectively). This observation suggests that higher temperatures lead the effective diffusivity ratios toward the value $D_{\mathrm{CH_4,b}}/D_{j,\mathrm{b}}$.

Role of pore structure and active area on washcoat performance

The washcoat performance under reacting conditions for different catalytic structures is herein evaluated considering the 3D multiscale and the 1D pseudohomogeneous washcoat models. For simplicity, the mixture composition at the external washcoat surface is set equal to the fresh mixture composition provided to the full-scale reactor. A temperature equal to 900 K is considered.

Figure 7 presents the 3D multiscale reaction-diffusion model results for the mole fraction and net production rate of CH_4 in the structures S^{15}_{a-A}, S^{15}_{c-A}, S^{15}_{c-C}, S^{15}_{b-B}, and S^{5}_{b-B}. These catalyst structures were selected to observe the sole effect of the mesoporous and macroporous structures, and catalyst loading/dispersion. An average simulation execution time between 3 and 7 days—in parallel (12 cores) with Intel® Xeon® processor E5–2620V2 units—was required to achieve a converged solution. In Figure 7, secondary gradients along transverse directions to the layer thickness are observed for structures with lower mesoporosity (compare the structures S^{15}_{x-A}), and higher macroporosities (compare the structures S^{15}_{c-X}). An increase in the active surface area also promotes the species transport in transverse directions (compare the structures $S^{F_{cat/geo}}_{b-B}$). The wider range of values observed for the structure S^{15}_{a-A} in relation to the remaining structures suggests that mass transport limitations are more severe for the structure S^{15}_{a-A}.

Figures 8a, b present gas species mole fraction profiles computed with the 3D multiscale and 1D pseudohomogeneous models along the thickness of washcoat layers. Particularly, Figure 8a encompasses the structures considered in Figure 7 concerning the CH_4 performance, while Figure 8b considers all reactive species for the structure S^{15}_{b-B}. In Figure 8a, a general good matching between the results (mole fraction profiles and effectiveness factors) predicted by both models is observed. Such agreement reinforces the ability of the 1D pseudohomogeneous model to accurately predict the washcoat performance under reacting conditions. The agreement between models is also registered for the remaining species, as presented in Figure 8b. In this figure, two regimes for methane

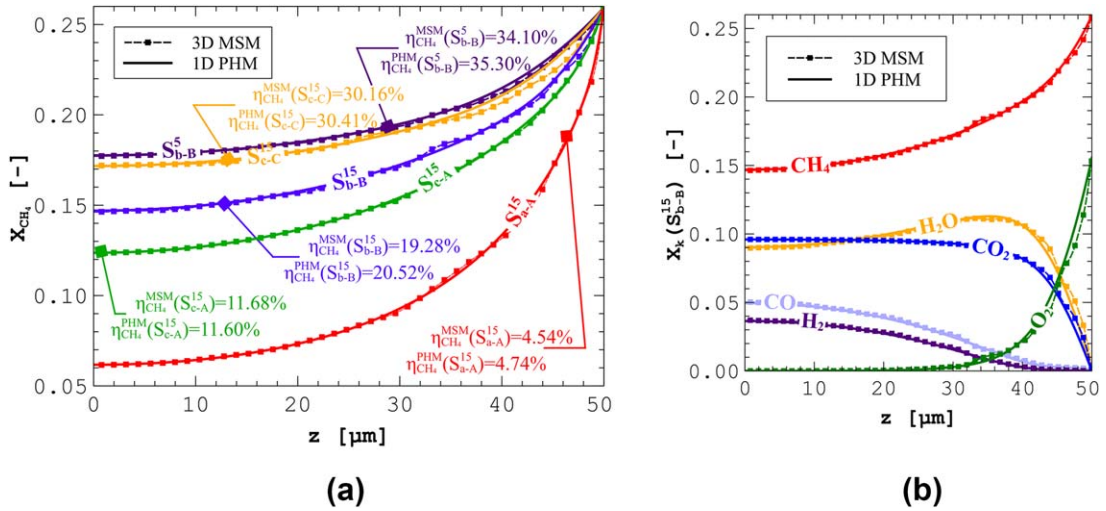

Figure 8. Species mole fraction profiles along the washcoat thickness evaluated with the 3D multiscale and 1D PHM: (a) CH_4 profiles (and effectiveness factors) for different combined structures; (b) all reactive species profiles for the structure S^{15}_{b-B}.

[Color figure can be viewed at wileyonlinelibrary.com]

consumption are observed along the washcoat thickness. Along the first 20 μm from the external surface, CH_4 is preferentially consumed with O_2 producing large amounts of H_2O and CO_2. When the O_2 becomes scarce, the remaining CH_4 mixture content continues to be consumed (at a slower pace) with the H_2O produced earlier to generate H_2 and CO. As H_2O is first produced and then consumed (through consecutive reactions), a maximum for the H_2O mole fraction profile is registered within the washcoat layer.

Figures 9a and 9b present the role of different effective transport and catalytic parameters on the methane effectiveness factor and average consumption rate, respectively. (Henceforward, references to η_k and $\dot{\omega}_k^{avg}$ are related with the application of 1D PHM.) In Figure 9a, the effectiveness factor is presented as a function of the ratio $a^{M,T}_{V,cat}/D^{M,eff}_{CH_4}$ for the effective diffusivity ratios characteristic of the structure S_{b-B}. For other effective diffusivity ratios, the effectiveness factors are presented in relation to those of the structure S_{b-B}. The

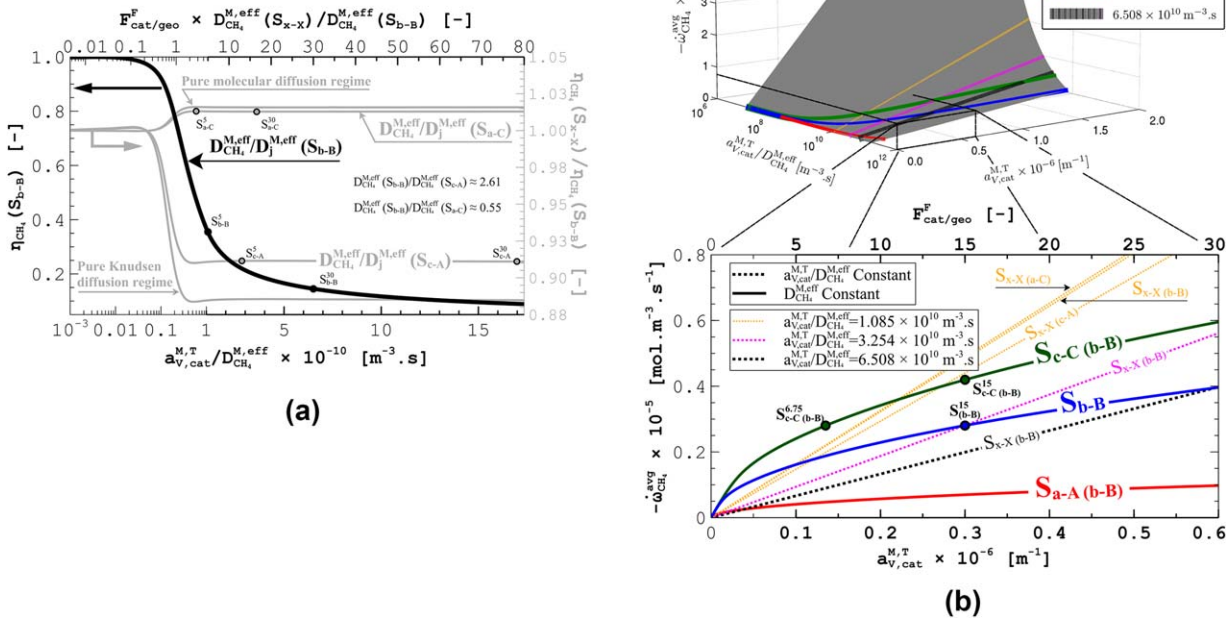

Figure 9. Washcoat performance for different effective transport properties and active surface areas concerning CH_4 consumption: (a) effectiveness factors; (b) average consumption rates.

[Color figure can be viewed at wileyonlinelibrary.com]

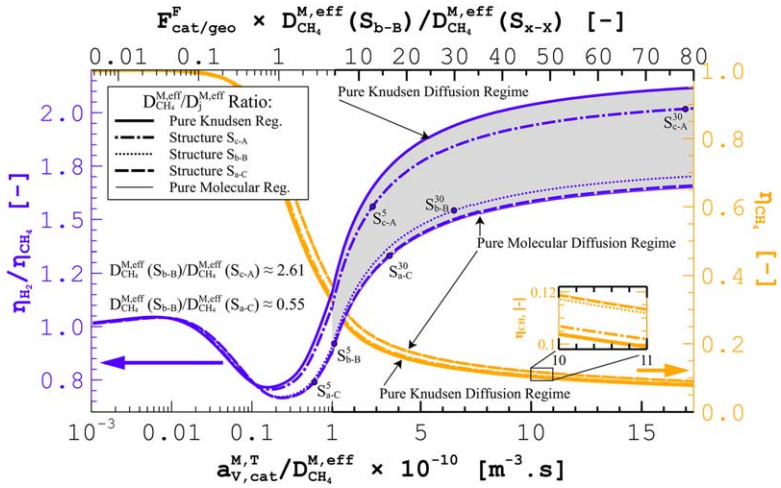

Figure 10. Washcoat performance for different effective transport properties and active surface areas concerning the H_2 production relative to the CH_4 consumption rates.

[Color figure can be viewed at wileyonlinelibrary.com]

lower inset of Figure 9b is a projection on the plane $-\dot{\omega}^{avg}_{CH_4} \times a^{M,T}_{V,cat}$ of the average consumption rate profiles that are presented in the upper inset (3D plot). The lower inset is also accompanied by complementary data. Structures $S_{x_1-X_1(x_2-X_2)}$ are fictitious structures with $D^{M,eff}_{CH_4}$ and $D^{M,eff}_{CH_4}/D^{M,eff}_{j}$ equal to $D^{M,eff}_{CH_4}(S_{x_1-X_1})$ and $D^{M,eff}_{CH_4}/D^{M,eff}_{j}(S_{x_2-X_2})$, respectively.

Along the $F^{F}_{cat/geo}$ range of practical interest (5–30) and for a constant set of effective diffusivity ratios, Figure 9a shows that an increase of the methane effectiveness factor is observed as the ratio $a^{M,T}_{V,cat}/D^{M,eff}_{CH_4}$ is decreased. For a particular porous structure, this can only be achieved decreasing the catalyst loading/dispersion. Although, an active surface area decrease is also liable for a decrease of the methane average consumption rate, as Figure 9b suggests. A simultaneous increase of the effectiveness factor and average consumption rate can only be pursuit through an increase of the effective diffusivity values by considering alternative porous structures. Furthermore, an increase in the effective diffusivities combined with a reduction (or increase) in the active surface area can still result in a catalyst structure operating with higher effectiveness factors and average consumption rates. For instance, the structure $S_{c-C(b-B)}$ with a $F^{F}_{cat/geo}$ value within the range]6.75,33.79[attains higher effectiveness factors and average consumption rates than those observed for the structure S^{15}_{b-B}—see the lower inset of Figure 9b.

The effect of the ratios $D^{M,eff}_{CH_4}/D^{M,eff}_{j}$ has also to be taken into account on the effectiveness factor. Over the $F^{F}_{cat/geo}$ range of interest and for a constant ratio $a^{M,T}_{V,cat}/D^{M,eff}_{CH_4}$, Figure 9a shows that the methane effectiveness factor increases as the structure's effective diffusivity ratios decrease, that is, as the species transport proceeds increasingly through the molecular diffusion regime. This is mainly due to the increase of the ratio $D^{M,eff}_{O_2}/D^{M,eff}_{CH_4}$ that promotes a higher methane consumption rate through total and partial oxidation reactions. As a consequence of the coupled behavior between $D^{M,eff}_{CH_4}$ and $D^{M,eff}_{CH_4}/D^{M,eff}_{j}$ as the pore structure changes (see Figure 5b), for a constant active surface area, an increase on $D^{M,eff}_{CH_4}$ promoted by an increase of the macroporosity leads to higher methane effectiveness factors (and average consumption rates) than an equal increase on $D^{M,eff}_{CH_4}$ but supported by an increase of the mesoporosity.

Figure 10 presents the role of the species effective transport properties and active surface area on the ratio η_{H_2}/η_{CH_4}. This ratio is proportional to the ratio $\dot{\omega}^{avg}_{H_2}/\dot{\omega}^{avg}_{CH_4}$ and, consequently, to the instantaneous H_2 selectivity. At a local (microscale) level, a higher ratio η_{H_2}/η_{CH_4} is preferred for the purpose of hydrogen production as methane becomes primarily converted into H_2 instead of H_2O. At a global (macroscale) level, the overall H_2 selectivity depends not only on the local values of η_{H_2}/η_{CH_4}, but also on the local values of methane consumption rates. In the $F^{F}_{cat/geo}$ range of practical interest, Figure 10 shows that an increase of the ratio η_{H_2}/η_{CH_4}—explained by a progressive promotion of the slow reforming reactions over the very fast oxidation reactions—is registered on increasing the ratio $a^{M,T}_{V,cat}/D^{M,eff}_{CH_4}$ and/or increasing the effective diffusivity ratios. Consequently, a specific increase of CH_4 consumption rates promoted by an increase on the active surface area instead of an increase (decrease) on the effective diffusivities (effective diffusivity ratios) allows to obtain a higher H_2 production rate (for the same fuel consumption rate), however, under stronger diffusion limitations. An increase of the ratio η_{H_2}/η_{CH_4} (and $\dot{\omega}^{avg}_{CH_4}$) results in a local (and global) enhancement of an apparent direct route for methane conversion into synthesis gas. The results of Figure 10 also suggest that replacing the application of the washcoat model by a fine-tuned active surface area to account for the effect of transport limitations on the CH_4 consumption rates leads to erroneous predictions for the H_2 production rates. This conclusion is drawn because ratios η_{H_2}/η_{CH_4} different than one—implying values for $\dot{\omega}^{avg}_{H_2}/\dot{\omega}^{avg}_{CH_4}$ different than $\dot{\omega}^{bnd}_{H_2}/\dot{\omega}^{bnd}_{CH_4}$—are registered in Figure 10.

Role of washcoat properties on reactor performance

The effect of washcoat transport properties and catalyst loading/dispersion on the full-scale reactor operation is herein analyzed. Figures 11a–d present temperature and species profiles along the reactor main flow direction for different porous structures with a constant active surface area (Figures 11a, b) and for different metal loadings (or dispersions) on a specific structure (Figures 11c, d). For each catalytic structure two sets of profiles are presented: one set considering internal diffusion

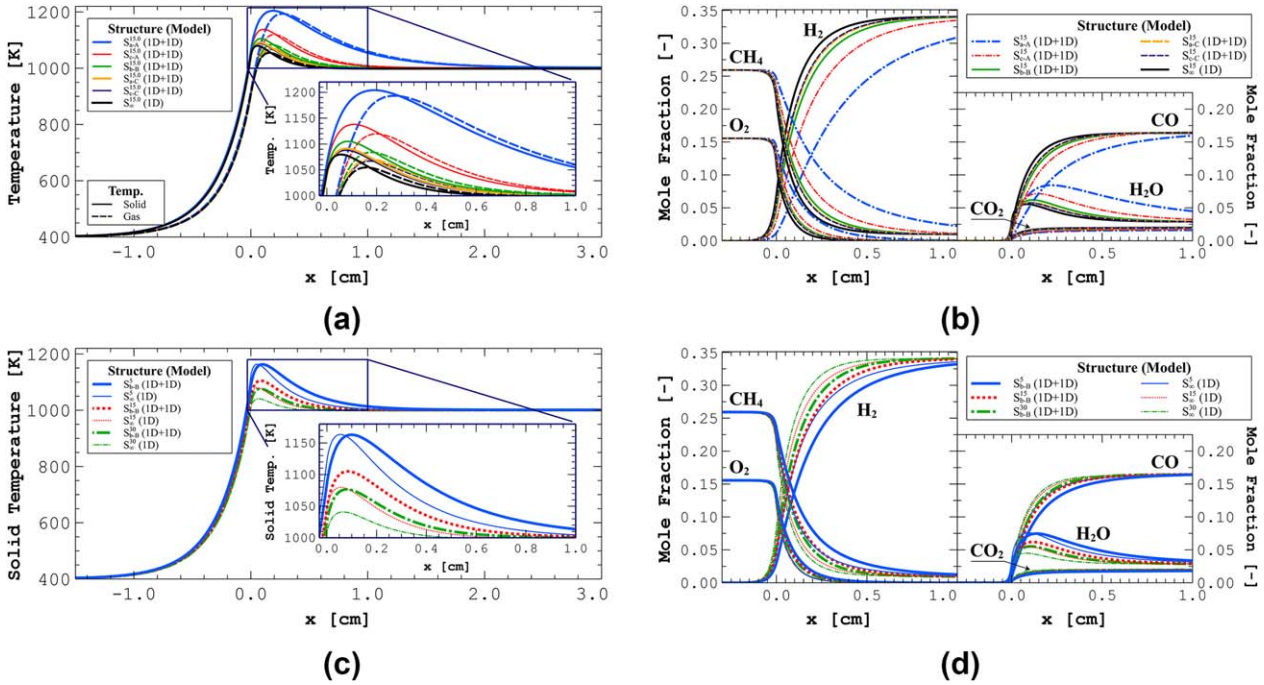

Figure 11. Full-scale reactor performance for washcoat layers with different pore structures but constant catalytic surface area ($F^{F}_{cat/geo}$=15)—(a) and (b)—and with different catalyst loadings/dispersions (different $F^{F}_{cat/geo}$ values) applied on the structure S_{b-B}—(c) and (d): (a) and (c) temperature profiles; (b) and (d) bulk species distribution profiles.

[Color figure can be viewed at wileyonlinelibrary.com]

limitations (according to the 1D + 1D model) and the other neglecting internal limitations (1D model). For clarity reasons, only five structures are considered in Figures 11a, b. In Figures 11a–d et seq., the front face of the active bed is located at $x = 0.0$ cm.

In Figures 11a–d, the differences on the reactor performance are particularly noticeable near the inlet section of the catalyst monolith (far from the thermodynamic control). Figure 11a shows that gradually higher temperatures are obtained as the washcoat effective diffusivities decrease. Moreover, the reactor axial location where the maximum temperatures are registered is shifted downstream for pore structures with lower effective diffusion coefficients. Figure 11c shows that as the active surface area is increased the temperatures decrease, being such decrease more pronounced when internal limitations are negligible. A gradual decrease of the catalyst loading/dispersion applying the 1D + 1D model leads to less sharp temperature excursions and to a maximum temperature shift toward the reactor exit section in relation to the 1D model results. Downstream the catalyst inlet section, the temperatures of the 1D + 1D model are higher than those predicted by the 1D model.

Regarding the product distribution profiles (Figures 11b, d), an axial slower response for the consumption/production of species is in accordance with higher catalyst temperatures. This is because the slower response is ascribed to lower observed rates from reforming (endothermic) reactions once the oxidation reactions taking place upstream are generally outside the control of kinetics—internal transport, and therefore, independent of the catalytic structure. However, noteworthy deviations between the O_2 mole fraction profiles for the structures $S^{15}_{\{a,c\}-A}$ and the remaining structures are shown in Figure 11b. These deviations go against the external-transport-controlled regime acknowledged for the bulk O_2 consumption with convenient catalyst structures and under conditions of practical relevance to perform catalytic partial oxidation of methane.[59,60] As such, the combined structures composed by the macroporous structure S_A (structures S_{x-A}) are not as suitable as the remaining structures to carry out the process because the O_2 conversion becomes limited by the extremely weak washcoat transport characteristics that are ultimately responsible for hindering the access of reactants to the active sites.

The comparison between the reactor performance observed for the structures S_{x-A} and the remaining structures (Figures 11a, b) presents common features with the behavior described during ongoing catalyst deactivation regimes, namely due to thermally induced deactivation mechanisms. Particularly, higher temperatures, lower CH_4 and O_2 conversions, and lower synthesis gas selectivities have been reported with deactivated catalyst foams due to metal sintering.[61] A progressive shift toward the reactor outlet of the maximum temperature values has also been reported as a result of catalyst aging.[62,63] Moreover, the resemblance between the performance of the structures S_{x-A} (in relation to the remaining structures) with the performance of deactivated catalyst samples is consistent with the fact that the macroporous structure S_A in relation to the remaining structures can be readily recognized as a structure that has undergone structural changes (triggered by high temperature exposure). This is because after structural modifications a structure with lower porosity and lower internal surface area is obtained, in which most of the active particles that were once available at the macropores' walls are encapsulated (inaccessible) within the microparticles' internal structure (collapsed macropores).[64,65]

Figures 12a–c present for different species and catalytic structures the mole fraction contours in the washcoat layer

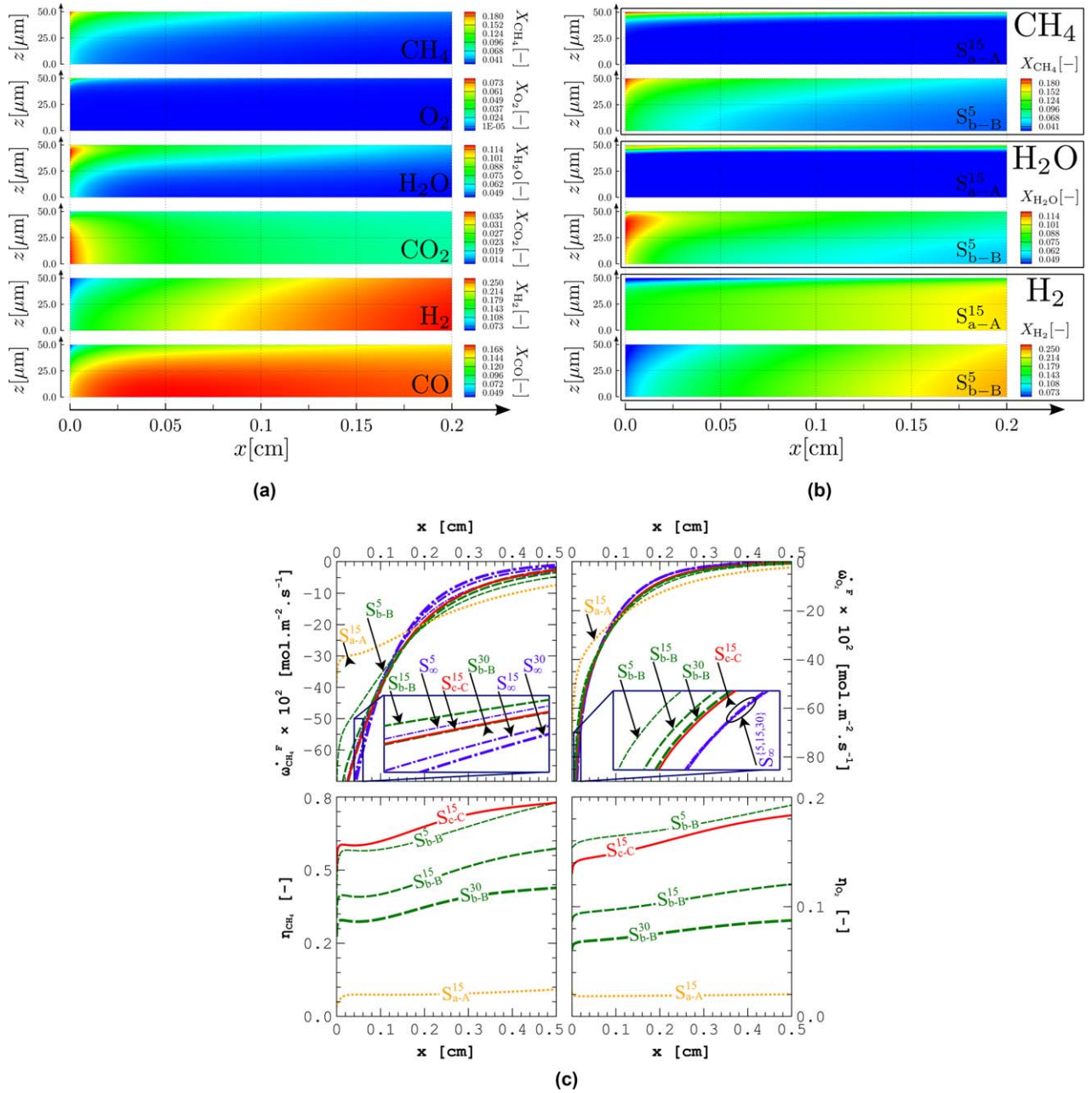

Figure 12. Full-scale reactor performance at the washcoat level: (a) and (b) mole fractions in the washcoat layer along the reactor first 0.2 cm for all reactive species with the structure S^{15}_{b-B} (a), and for CH_4, H_2O and H_2 with the structures S^{15}_{a-A} and S^{5}_{b-B} (b); (c) net production rates and effectiveness factors for CH_4 and O_2 with the structures S^{15}_{a-A}, $S^{\{5,15,30\}}_{b-B}$, and S^{15}_{c-C}.

[Color figure can be viewed at wileyonlinelibrary.com]

along the first 0.2 cm of the catalyst monolith (Figures 12a, b), and the net production rates and effectiveness factors (Figure 12c). In Figure 12a, the steep species mole fraction gradients observed along the washcoat thickness in the first few millimeters of the catalyst bed suggest an important relevance of internal transport limitations near the reactor entrance. This is in full accordance with the lower effectiveness factors for CH_4 and O_2 therein observed (see Figure 12c). This behavior is due to the extremely fast oxidation reactions expected at the beginning of the catalyst bed that become more penalized by transport limitations than the slower reactions taking place downstream. The oxygen is completely consumed in the outermost region of the washcoat layer. A maximum for the H_2O mole fraction is observed near the catalyst entrance (oxidation zone) due to the consecutive oxidation/reforming reactions along the washcoat thickness. This evidence is in line with previous results (see Figure 8b). Further downstream where the O_2 becomes absent at the external washcoat surface (reforming zone), the H_2O mole fraction profiles along the washcoat thickness become monotonically decreasing.

The influence of the transport properties and active surface area on the mole fraction contours of CH_4, H_2O and H_2 can be observed considering the structures S^{15}_{a-A} (Figure 12b) and S^{15}_{b-B} (Figure 12a), and the structures S^{5}_{b-B} (Figure 12b) and

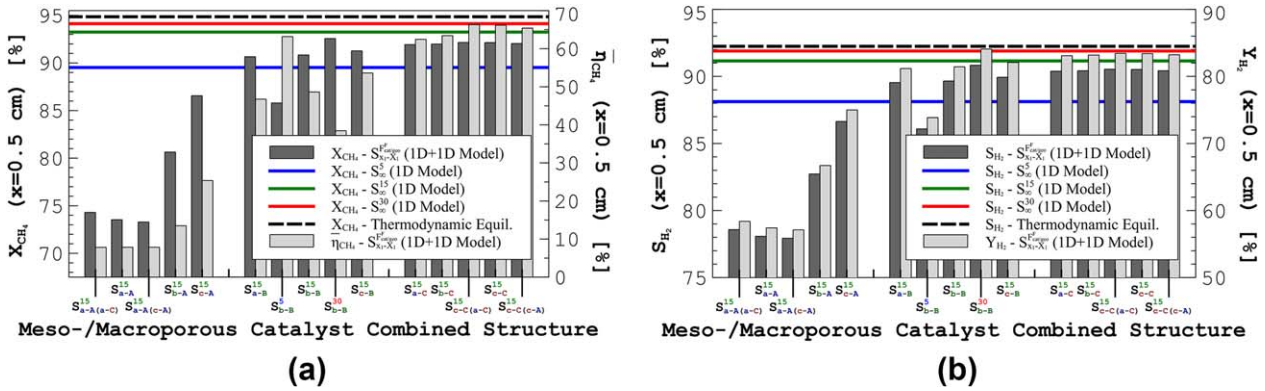

Figure 13. Full-scale reactor performance parameters evaluated with the 1D + 1D model and with the 1D model: (a) CH_4 conversion (X_{CH_4}) and average effectiveness factor ($\bar{\eta}_{CH_4}$); (b) H_2 selectivity (S_{H_2}) and yield (Y_{H_2}).

[Color figure can be viewed at wileyonlinelibrary.com]

S^{15}_{b-B}, respectively. As the effective diffusivities increase (catalytic surface area decreases), the mole fraction gradients along the washcoat thickness decrease and, consequently, the effectiveness factors increase (see Figure 12c). For the structure S^{15}_{a-A}, Figures 12b, c reveal that the majority of the washcoat thickness is not accessible for reactant species conversion due to the low species penetration depth. Moreover, due to the significantly lower O_2 average consumption rates observed for the catalyst structure S^{15}_{a-A} (suggested by Figure 11b and supported by Figure 12c), the oxidation zone extends further downstream the catalyst bed and, therefore, the maximum on the H_2O mole fraction along the washcoat thickness is observed over a longer axial distance in relation to the remaining structures.

Figures 13a and 13b present the CH_4 fractional conversion and average effectiveness factor, and the H_2 selectivity and yield, respectively, evaluated at the reactor axial position x=0.5 cm for the nine catalyst bimodal structures and also for several fictitious structures (structures $S^{F^{cat/geo}}_{x_1-X_1(x_2-X_2)}$). Higher methane conversion and hydrogen selectivity values are observed for structures with higher effective diffusivities, higher catalyst loadings/dispersions, and lower effective diffusivity ratios. The role played by the effective diffusivity ratios becomes more visible for structures operating under stronger diffusion limitations (compare the performance of the structures $S^{15}_{a-A(x-X)}$ and $S^{15}_{c-C(x-X)}$). Methane conversion follows the same trends with washcoat properties as the methane average consumption rates (see Figure 9). Regarding the hydrogen selectivity, even though a decrease (increase) of the effective diffusivities (effective diffusivity ratios) results in a promotion of the instantaneous hydrogen selectivity (see the ratio η_{H_2}/η_{CH_4} in Figure 10), at the full-scale reactor level this trend results in a decrease of the integral hydrogen selectivity. This is observed because the increase of the instantaneous hydrogen selectivity with the effective transport properties is registered alongside a significant decrease of the average fuel consumption rates (see Figure 9). The decrease of the CH_4 consumption rates at the beginning of the catalyst bed—expected decreasing the effective transport properties (see Figure 12c)—is responsible for delaying reforming reactions until the O_2 content in the bulk gas mixture becomes negligible. This mechanism promotes a progressive spatial decoupling between oxidation and reforming reactions for structures with lower effective diffusivities (higher effective diffusivity ratios), that is in full accordance with: (1) the late axial heat consumption observed through higher and shifted downstream temperatures (see Figure 11a); and (2) the lower H_2 yields (see Figure 13b).

Methane conversion and hydrogen selectivity evaluated considering internal limitations are as close to the values predicted neglecting limitations as the effective diffusivities and active surface area increase. This evidence is in agreement with the lower contact times (shorter reactors) that are required to reach the thermodynamic equilibrium by increasing the effective diffusivities and catalyst loading/dispersion (see Figures 11a–d). These trends on effective diffusivities and active surface area are responsible for weakening the effects of pore diffusion on the overall regime governing the macroscale performance, in such a way that the full-scale reactor becomes gradually controlled by the regimes observed in the absence of diffusion limitations: external transport of O_2 for the oxidation reactions[59,60] and a mixed external transport–kinetic regime for CH_4 consumption through reforming reactions.[60,66]

Figure 14 presents the hydrogen yield at x=0.5 cm for all porous structures considering a constant ratio between active and geometric surface areas at the nanoscale level ($F^{m}_{cat/geo}$). A constant $F^{m}_{cat/geo}$ value—that can be understood as a constant metal dispersion—applied in samples with different surface areas ($A^{M,T}_{geo}$) leads to a different total active surface area (and catalyst loading) for each sample. Structures with higher porosities have simultaneously higher effective diffusivities and lower active surface areas—lower $F^{F}_{cat/geo}$ ($=F^{m}_{cat/geo}A^{M,T}_{geo}/$

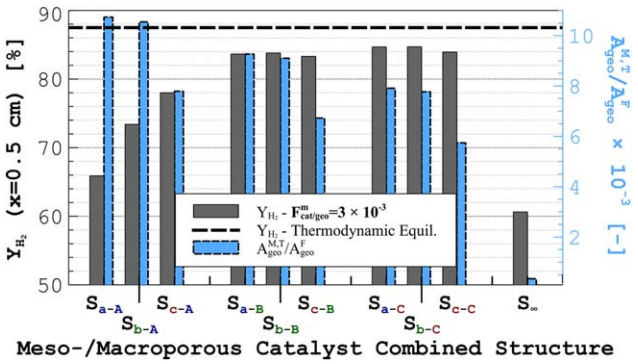

Figure 14. H_2 yield evaluated at the reactor position x= 0.5 cm for all combined structures considering a constant $F^{m}_{cat/geo}$ value.

[Color figure can be viewed at wileyonlinelibrary.com]

A^{F}_{geo}) values. Therefore, an increase of the mesoporosity (macroporosity) for a particular macroporous (mesoporous) structure only results in an enhancement of the H_2 yield if the increase of the effective diffusivities overcomes the corresponding decrease in the active surface area. This is observed for the structures $S_{\{a,b,c\}-A}$ (mesoporosity increase) and $S_{x-\{A,B,C\}}$ (macroporosity increase). Figure 14 also presents the H_2 yield achieved considering a very thin washcoat layer ($\delta^{M}_{z}=3$ μm) with a specific surface area equal to that of structure S_{c-C} and in which the diffusion limitations are neglected – *structure* S_{∞}. The comparison of the results obtained for this *structure* against those observed for the remaining structures illustrates well the need for a washcoat application. The reactor performance would be even worse (and unacceptable) if the active ingredients were deposited directly onto the bare honeycomb cordierite walls.

Conclusion

This work reports the application of a multiscale methodology to a honeycomb reactor performing methane catalytic partial oxidation. The multiscale methodology embraces three reactor length-scales (nanoscale, microscale, and macroscale levels) and requires consecutive pore-scale simulations organized according to a hierarchical bottom-up approach. The role of washcoat pore structure and active surface area on the catalyst layer and reactor performances is investigated. Mesoporous and macroporous structures were virtually reconstructed with realistic morphological parameters.

The results show that effective diffusivities increase with an increase in the mesoporosity/macroporosity. Species diffusion through mesopores becomes less relevant at higher temperatures and for samples with lower (higher) mesoporosity (macroporosity). Under reactive conditions, the reliability of the overall multiscale methodology is supported on the good agreement registered between the results of the 3D multiscale and 1D pseudohomogeneous reaction-diffusion models. A more selective route toward hydrogen production (at microscale and macroscale levels) is noticed promoting a preferential increase in the active surface area than in the effective diffusivities for the same methane consumption rate. The full-scale reactor level results show that an increase of methane conversion and hydrogen selectivity—toward the values obtained without diffusion limitations—is observed for structures with higher effective diffusivities and higher active surface areas. Structures with extremely poor transport properties present low species penetration depths along the washcoat layer (low catalyst utilization levels) which may affect the typical regimes controlling the reactor performance. Neglecting internal diffusion limitations for these structures results in underpredicted (and upstream-shifted) temperature profiles.

The multiscale methodology applied in this work provides a reliable and feasible strategy to transport the effect of morphological and catalytic details from the mesopore and macropore to the full-scale reactor operation. This methodology can be applied for catalyst optimization studies to support the development of improved pore structures and catalyst distribution profiles.

Acknowledgments

This work was supported by FCT, through IDMEC, under LAETA, project UID/EMS/50022/2013.

Literature Cited

1. de Smet CRH, de Croon MHJM, Berger RJ, Marin GB, Schouten JC. Design of adiabatic fixed-bed reactors for the partial oxidation of methane to synthesis gas. Application to production of methanol and hydrogen-for-fuel-cells. *Chem Eng Sci*. 2001;56:4849–4861.
2. York APE, Xiao T, Green MLH. Brief overview of the partial oxidation of methane to synthesis gas. *Top Catal*. 2003;22:345–358.
3. Groppi G, Beretta A, Tronconi E. Monolithic catalysis for gas-phase syntheses of chemical, chap. 8. In: Cybulski A, and Moulijn JA, editors. *Structured Catalysts and Reactors*. CRC Press, 2005:243–310. Available from https://www.crcpress.com/Structured-Catalysts-and-Reactors/Cybulski-Moulijn/p/book/9780824723439.
4. Holladay JD, Hu J, King DL, Wang Y. An overview of hydrogen production technologies. *Catal Today*. 2009;139:244–260.
5. Bharadwaj SS, Schmidt LD. Catalytic partial oxidation of natural gas to syngas. *Fuel Process Technol*. 1995;42:109–127.
6. Williams KA, Leclerc CA, Schmidt LD. Rapid lightoff of syngas production from methane: a transient product analysis. *AIChE J*. 2005;51:247–260.
7. Vernon PDF, Green MLH, Cheetham AK, Ashcroft AT. Partial oxidation of methane to synthesis gas. *Catal Letters*. 1990;6:181–186.
8. Liu K, Deluga GD, Bitsch-Larsen A, Schmidt LD, Zhang L. Catalytic partial oxidation and autothermal reforming, chap. 3. In: Liu K, and Subramani V, editors. *Hydrogen and Syngas Production and Purification Technologies*. John Wiley & Sons, 2009:127–155. Available from http://onlinelibrary.wiley.com/book/10.1002/9780470561256.
9. Claridge JB, Green MLH, Tsang SC, York APE, Ashcroft AT, Battle PD. A study of carbon deposition on catalysts during the partial oxidation of methane to synthesis gas. *Catal Letters*. 1993;22:299–305.
10. Nematollahi B, Rezaei M, Khajenoori M. Combined dry reforming and partial oxidation of methane to synthesis gas on noble metal catalysts. *Int J Hydrogen Energy*. 2011;36:2969–2978.
11. Enger BC, Lødeng R, Holmen A. A review of catalytic partial oxidation of methane to synthesis gas with emphasis on reaction mechanisms over transition metal catalysts. *Appl Catal A Gen*. 2008;346:1–27.
12. Deutschmann O. Catalytic reforming of logistic fuels at high-temperatures. In: Spivey JJ, Gupta M, editors. *Catalysis*, vol. 24. The Royal Society of Chemistry, 2012:48–82. Available from http://pubs.rsc.org/en/content/chapter/bk9781849733755-00048/978-1-84973-375-5.
13. Beretta A, Donazzi A, Groppi G, Maestri M, Tronconi E, Forzatti P. Gaining insight into the kinetics of partial oxidation of light hydrocarbons on Rh, through a multiscale methodology based on advanced experimental and modeling techniques. In: Spivey JJ, Dooley KM, Han YF, editors. *Catalysis*, vol. 25. The Royal Society of Chemistry, 2013:1–49. Available from http://pubs.rsc.org/en/content/chapter/bk9781849735780-00001/978-1-84973-578-0.
14. Hayes RE, Kolaczkowski ST. *Introduction to Catalytic Combustion*. Amsterdam: Gordon and Breach Science, 1997.
15. Holder R, Bolling M, Anderson DR, Hochmuth JK. A discussion on transport phenomena and three-way kinetics of monolith converters. *Chem Eng Sci*. 2006;61:8010–8027.
16. Depcik C, Srinivasan A. One + one-dimensional modeling of monolithic catalytic converters. *Chem Eng Technol*. 2011;34:1949–1965.
17. Janardhanan VM, Deutschmann O. *Computational Fluid Dynamics of Catalytic Reactors*. Wiley-VCH Verlag GmbH, 2011:251–282.
18. Froment GB, Bischoff KB. *Chemical Reactor Analysis and Design*. New York: John Wiley & Sons, 1990.
19. Hauff K, Boll W, Tischer S, Chan D, Tuttlies U, Eigenberger G, Deutschmann O, Nieken U. Macro- and microkinetic simulation of diesel oxidation catalyst: effect of aging, noble metal loading and platinum oxidation. *Chem Ing Tech*. 2013;85:673–685.
20. Papadias D. *Mathematical Modeling of Structured Reactors - Emphasis on Catalytic Combustion Reactions*. Germany: VDM Publishing House, 2009.
21. Mladenov N, Koop J, Tischer S, Deutschmann O. Modeling of transport and chemistry in channel flows of automotive catalytic converters. *Chem Eng Sci*. 2010;65:812–826.
22. Leung D, Hayes RE, Kolaczkowski ST. Diffusion limitation effects in the washcoat of a catalytic monolith reactor. *T Can J Chem Eng*. 1996;74:94–103.
23. Hayes RE, Liu B, Votsmeier M. Calculating effectiveness factors in non-uniform washcoat shapes. *Chem Eng Sci*. 2005;60:2037–2050.
24. Pagani D, Livio D, Donazzi A, Beretta A, Groppi G, Maestri M, Tronconi E. A kinetic analysis of the partial oxidation of C_3H_8 over a 2% Rh/Al_2O_3 catalyst in annular microreactor. *Catal Today*. 2012;197:265–280.

25. Karadeniz H, Karakaya C, Tischer S, Deutschmann O. Numerical modeling of stagnation-flows on porous catalytic surfaces: CO oxidation on Rh/Al_2O_3. *Chem Eng Sci*. 2013;104:899–907.
26. Johannessen E, Wang G, Coppens MO. Optimal distributor networks in porous catalyst pellets. I. Molecular diffusion. *Ind Eng Chem Res*. 2007;46:4245–4256.
27. Wang G, Johannessen E, Kleijn CR, de Leeuw SW, Coppens MO. Optimizing transport in nanostructured catalysts: a computational study. *Chem Eng Sci*. 2007;62:5110–5116.
28. Wang G, Coppens MO. Rational Design of hierarchically structured porous catalysts for autothermal reforming of methane. *Chem Eng Sci*. 2010;65:2344–2351.
29. Nanjundappa A, Alavijeh AS, Hannach ME, Harvey D, Kjeang E. A customized framework for 3-D morphological characterization of microporous layers. *Electrochim Acta*. 2013;110:349–357.
30. Novák V, Kočí P, Štěpánek F, Marek M. Integrated multiscale methodology for virtual prototyping of porous catalysts. *Ind Eng Chem Res*. 2011;50:12904–12914.
31. Becker J, Wieser C, Fell S, Steiner K. A multi-scale approach to material modeling of fuel cell diffusion media. *Int J Heat Mass Transf*. 2011;54:1360–1368.
32. Naseri AT, Peppley BA, Pharoah JG. Computational analysis of the reacting flow in a microstructured reformer using a multiscale approach. *AIChE J*. 2014;60:2263–2274.
33. Pereira JMC, Navalho JEP, Amador ACG, Pereira JCF. Multi-scale modeling of diffusion and reaction-diffusion phenomena in catalytic porous layers: comparison with the 1D approach. *Chem Eng Sci*. 2014;117:364–375.
34. Novák V, Kočí P, Gregor T, Choi J, Štěpánek F, Marek M. Effect of cavities and cracks on diffusivity in coated catalyst layer. *Catal Today*. 2013;216:142–149.
35. Navalho JEP, Pereira JMC, Pereira JCF. Multi-scale modeling of internal mass diffusion limitations in CO oxidation catalysts. *Defect Diffus Forum*. 2015;364:92–103.
36. Zamel N, Becker J, Wiegmann A. Estimating the thermal conductivity and diffusion coefficient of the microporous layer polymer electrolyte membrane fuel cells. *J Power Sources*. 2012;207:70–80.
37. Dudák M, Novák V, Kočí P, Marek M, Blanco-García P, Jones G. Prediction of diffusivity and conversion of *n*-decane and CO in coated $Pt/\gamma-Al_2O_3$ catalyst depending on porous layer morphology. *Appl Catal B Environ*. 2014;150–151:446–458.
38. Votsmeier M. Efficient implementation of detailed surface chemistry into reactor models using mapped rate data. *Chem Eng Sci*. 2009;64:1384–1389.
39. Seyed-Reihani SA, Jackson GS. Effectiveness in catalytic washcoats with multi-step mechanisms for catalytic combustion of hydrogen. *Chem Eng Sci*. 2004;59:5937–5948.
40. von Rickenbach J, Lucci F, Narayanan C, Eggenschwiler PD, Poulikakos D. Effect of washcoat diffusion resistance in foam based catalytic reactors. *Chem Eng J*. 2015;276:388–397.
41. Tronconi E, Nova I, Ciardelli C, Chaterjee D, Bandl-Konrad B, Burkhardt T. Modelling of an SCR catalytic converter for diesel exhaust after treatment: dynamic effects at low temperature. *Catal Today*. 2005;105:529–536.
42. Shakya BM, Harold MP, Balakotaiah V. Modeling and analysis of dual-layer NO_x storage and reduction and selective catalytic reduction monolithic catalyst. *Chem Eng J*. 2014;237:109–122.
43. Kočí P, Štěpánek F, Kubíček M, Marek M. Modelling of micro/nano-scale concentration and temperature gradients in porous supported catalysts. *Chem Eng Sci*. 2007;62:5380–5385.
44. Novák V, Štěpánek F, Kočí P, Marek M, Kubíček M. Evaluation of local pore sizes and transport properties in porous catalysts. *Chem Eng Sci*. 2010;65:2352–2360.
45. Poling BE, Prausnitz JM, O'connel JP. *The Properties of Gases and Liquids*. McGraw-Hill Professional, 2000. Available from https://www.mhprofessional.com/9780070116825-usa-the-properties-of-gases-and-liquids-5e-group.
46. Navalho JEP, Frenzel I, Loukou A, Pereira JMC, Trimis D, Pereira JCF. Catalytic partial oxidation of methane rich mixtures in non-adiabatic monolith reactors. *Int J Hydrogen Energy*. 2013;38:6989–7006.
47. Navalho JEP, Pereira JMC, Ervilha AR, Pereira JCF. Uncertainty quantification in catalytic partial oxidation of methane. *Combust Theor Model*. 2013;17:1067–1095.
48. Kee RJ, Coltrin ME, Glarborg P. *Chemically Reacting Flow: Theory and Practice*. New Jersey: Wiley-Interscience, 2003.
49. Schwiedernoch R, Tischer S, Correa C, Deutschmann O. Experimental and numerical study on the transient behavior of partial oxidation of methane in a catalytic monolith. *Chem Eng Sci*. 2003;58:633–642.
50. Navalho JEP, Pereira JMC, Pereira JCF. Conical-shaped foam reactors for catalytic partial oxidation applications. *Int J Hydrogen Energy*. 2014;39:3666–3680.
51. Shah R, London A. *Laminar Flow Forced Convection in Ducts*. New York: Academic Press, 1978.
52. Karakaya C, Maier L, Deutschmann O. Surface reaction kinetics of the oxidation and reforming of CH_4 over Rh/Al_2O_3 catalysts. *Int J Chem Kinet*. 2016;48:144–160.
53. Goodwin DG. An open-source, extensible software suite for CVD process simulation. CVD XVI and EuroCVD Fourteen, Electrochemical Society. 2003:155–162.
54. Kee RJ, Grcar JF, Smooke MD, Miller JA. Premix: a Fortran program for modeling steady laminar one-dimensional premixed flames. *Tech. Rep. SAND85–8240*, Sandia National Laboratories, 1985.
55. dos Santos LOE, Philippi PC, Fernandes CP, de Gaspari HC. Three-dimensional reconstruction of porous microstructures with the superposed spheres method. In: *Proceedings of the ENCIT 2002,* Caxambu - MG, Brazil, CIT02–0449, 2002.
56. Hayes RE, Kolaczkowski ST, Li PKC, Awdry S. Evaluating the effective diffusivity of methane in the washcoat of a honeycomb monolith. *Appl Catal B Environ*. 2000;25:93–104.
57. Karakaya C, Otterstätter R, Maier L, Deutschmann O. Kinetics of the water-gas shift reaction over Rh/Al_2O_3 catalysts. *Appl Catal A Gen*. 2014;470:31–44.
58. Eriksson S, Schneider A, Mantzaras J, Wolf M, Järås S. Experimental and numerical investigation of supported rhodium catalysts for partial oxidation of methane in exhaust gas diluted reaction mixtures. *Chem Eng Sci*. 2007;62:3991–4011.
59. Horn R, Williams KA, Degenstein NJ, Bitsch-Larsen A, Dalle Nogare D, Tupy SA, Schmidt LD. Methane catalytic partial oxidation on autothermal Rh and Pt foam catalysts: oxidation and reforming zones, transport effects, and approach to thermodynamic equilibrium. *J Catal*. 2007;249:380–393.
60. Donazzi A, Maestri M, Michael BC, Beretta A, Forzatti P, Groppi G, Tronconi E, Schmidt LD, Vlachos DG. Microkinetic modeling of spatially resolved autothermal CH_4 catalytic partial oxidation experiments over Rh-coated foams. *J Catal*. 2010;275:270–279.
61. Ding S, Yang Y, Jin Y, Cheng Y. Catalyst deactivation of Rh-coated foam monolith for catalytic partial oxidation of methane. *Ind Eng Chem Res*. 2009;48:2878–2885.
62. Beretta A, Groppi G, Lualdi M, Tavazzi I, Forzatti P. Experimental and modeling analysis of methane partial oxidation: transient and steady-state behavior of Rh-coated honeycomb monoliths. *Ind Eng Chem Res*. 2009;48:3825–3836.
63. Gudlavalleti S, Ros T, Lieftink D. Thermal sintering studies of an autothermal reforming catalyst. *Appl Catal B Environ*. 2007;74:251–260.
64. Heck RM, Farrauto RJ, Gulati ST. *Catalytic Air Pollution Control: Commercial Technology*. Hoboken, New Jersey: John Wiley & Sons, 2009.
65. Argyle MD, Bartholomew CH. Heterogeneous catalyst deactivation and regeneration: a review. *Catalysts*. 2015;5:145–269.
66. Livio D, Donazzi A, Beretta A, Groppi G, Forzatti P. Experimental and modeling analysis of the thermal behavior of an autothermal C_3H_8 catalytic partial oxidation reformer. *Ind Eng Chem Res*. 2012;51:7573–7583.

Manuscript received Apr. 24, 2017, and revision received July 24, 2017.